

See discussions, stats, and author profiles for this publication at: <https://www.researchgate.net/publication/319594648>

# Terahertz Antennas and Feeds

Chapter · January 2018

DOI: 10.1007/978-3-319-62773-1\_10

---

CITATIONS  
0

READS  
222

6 authors, including:



Nacer Chahat  
NASA Jet Propulsion Laboratory

89 PUBLICATIONS 978 CITATIONS

[SEE PROFILE](#)



David Gonzalez-Ovejero  
French National Centre for Scientific Research

87 PUBLICATIONS 670 CITATIONS

[SEE PROFILE](#)



Choonsup Lee  
California Institute of Technology

120 PUBLICATIONS 1,840 CITATIONS

[SEE PROFILE](#)



T. Reck  
Virginia Diodes Inc.

98 PUBLICATIONS 785 CITATIONS

[SEE PROFILE](#)

Some of the authors of this publication are also working on these related projects:



MEMS Technology [View project](#)



Improved heterodyne receiving arrays for Teraherzt applications [View project](#)

# Chapter 11

## Terahertz antennas and feeds

Goutam Chattopadhyay  
Maria Alonso-delPino  
Nacer Chahat  
David González-Ovejero  
Choonsup Lee  
Theodore Reck

NASA Jet Propulsion Laboratory, California Institute of Technology, Pasadena, CA, USA

11.1.	Introduction.....	2
11.2.	Feed horn antennas.....	3
11.2.1.	Corrugated horns .....	5
11.2.2.	Multi-flare angle.....	10
11.2.2.1.	Optimization method .....	10
11.2.2.2.	1900 GHz multi-flare angle horn antenna.....	11
11.2.2.2.	TWICE multi-flare angle horn antenna.....	14
11.2.3.	Smooth-walled horn.....	17
11.3.	Lens antennas.....	19
11.3.1.	Introduction and State of the Art.....	19
11.3.2.	Silicon Micro-Lens Antennas Fed by Leaky-Wave Waveguide Feeds.....	20
11.3.3.	Fabrication and Assembly .....	23
11.3.4.	Fabrication of the Leaky Wave Waveguide Feed .....	24
11.3.5.	Fabrication of the Shallow Silicon Lens .....	24
11.3.6.	Silicon Micro-Lens antenna performance and limitations .....	26
11.4.	Terahertz modulated metasurface antennas.....	29
11.4.1	Sinusoidally Modulated Inductive Surfaces.....	29
11.4.2	Constituent Elements for THz metasurfaces .....	30
11.4.2	Design example .....	31
11.5.	CMOS antennas .....	33
11.6.	Slot antennas in BICEP2.....	37
11.7.	Conclusion .....	40
	Acknowledgement.....	40
	References.....	41

## 11.1. Introduction

Terahertz antennas present a different set of challenges to the antenna designer typically striving for very high performance while at the very limit of the chosen fabrication process. Many of the same design techniques used at lower frequencies are still applied, but fabrication constraints impose significant limitations on the type of structure that can be used, forcing the designer to consider unique fabrication processes or completely new antenna structures. Through advances in fabrication and computational techniques, the variety of terahertz antennas is growing. This chapter presents a range of antennas applied at these frequencies from 1.9THz horn antennas to superconducting planar arrays.

Horn antennas dominate terahertz systems because of the low-losses and excellent performance. In particular, corrugated horn antennas have superior radiation characteristics, but are difficult to fabricate at terahertz frequencies, thus one of the most commonly used horns above 300GHz is the diagonal horn antenna, despite its high cross-polarization. In addition to describing multi-mode horn designs such as the Pickett-Potter horn, Section 11.2 presents two approaches to overcoming fabrication obstacles for achieving high gain and low cross-polarization horns. The first relies on the stacking of platelets to form a corrugated horn. The second uses extensive optimization to create profiled horns that has been shown to be manufacturable as high as 1.9THz.

Lens coupled antennas have been widely used for decades in Terahertz systems because they avoid the high tolerances of horns. But their application is limited because Terahertz systems are often waveguide-based system. Section 11.3 describes the leaky-wave fed lens that directly couples to hollow-waveguide. In addition, the leaky-wave system reduces the area required for illumination area, increasing pixel-spacing for array systems and enabling a batch-fabrication process for forming the lenses.

Section 11.4 applies the emerging technique of modulated metasurface antennas, discussed in detail in Chapter 13, to Terahertz frequencies. These designs result in a planar antenna which are attractive for space-borne instruments because high gains can be achieve with less mass and volume than a comparable reflector system.

Planar Terahertz antennas are discussed in Sections 11.5 and 11.6. To avoid lossy on-chip antennas when coupling to CMOS components, membrane-suspended antennas are demonstrated in Section 11.5 that use beam-lead technology to couple directly to the CMOS wire-bond pads. Finally, a slot-array antenna is described that is used on Cosmic Microwave Background experiment that uses superconducting transmission lines for routing the large-format array.

## 11.2. Feed horn antennas

The most common use for horn antennas [1]-[4] at submillimeter-waves is to feed reflectors and/or quasi-optical systems [5]. Reflector antennas and Gaussian beam telescopes produce pencil beams, and to be effective, their gain has to be as high as possible within an acceptable side-lobe envelope. Therefore, in order to increase the spillover and aperture efficiencies, feed horns are required to have equalized beamwidths in all planes and low side-lobe levels. In addition, the reflector normally be required to transmit and receive orthogonally polarized waves, so one has to guarantee a low level of the cross-polar radiation patterns. Finally, for instruments involving complex optics and/or focal plane arrays for multiple beam operation it is also convenient to have good coupling to the fundamental Gaussian mode. These are the reasons why, over the years, there has been a need in Terahertz instruments for horn antennas which provide symmetric patterns in all planes, phase center coincidence for the E- and H-planes, side lobe suppression, low cross-polarized fields, and highly Gaussian beams.

Pyramidal horns have been widely used, with good success, in many applications. Such radiators, however, possess non-symmetric beamwidths and undesirable side-lobe levels, especially in the E-plane. Conical horns, operating in the dominant TE<sub>11</sub> mode, have a tapered aperture distribution in the E-plane. Thus, they exhibit more symmetric E- and H-plane beamwidths and lower side lobes than the pyramidal horns. Nevertheless, conical horns require appropriate transitions to make them compatible with a rectangular waveguide input. To overcome some of the limitations of pyramidal and conical horns, and further improve their attractive characteristics, horn structures with multiple-mode excitations have been suggested to enhance the beamwidth equalization in all planes, and to reduce both the sidelobe level and cross-polarized fields. By appropriately combining the fundamental mode in the waveguide with higher order modes, multimode horns allow one to tailor the field distribution at the horn aperture. This strategy can be used to generate highly symmetric beams with low side-lobe levels and low cross-polarized fields.



**Figure 11.1.** Pictures of a split-block diagonal horn with WR-1.5 input from Virginia Diodes. (a) Assembled blocks including the horn and integrated flange. (b) Upper and lower blocks, where one can also observe the dowel pins used for alignment.

Diagonal horns are, for its simplicity, one of the most popular feeds at submillimeter waves [6]-[7]. Figure 11.1 shows the picture of a diagonal horn with a rectangular WR-1.5 waveguide input. Its flared section consists of a pyramid which, at the throat of the horn, intersects a rectangular waveguide with its wide and narrow walls parallel to the diagonals of the pyramid's cross-section. Love [6] used a circular transition from a TE<sub>10</sub> mode, but the direct transition described above provides good performance with a relatively simple fabrication process. Figure 11.2a and Figure 11.2b show cross-sections through the block at various points along the transition. The field beyond the transition section consists of the superposition of two orthogonal TE<sub>10</sub> modes, having power equally distributed between them, as shown in Figure 11.3a. Bearing in mind the geometry in Figure 11.3b, one can write the electric field at the aperture of the horn as

$$\mathbf{E}_A = E_0 \left[ \cos\left(\frac{\pi y}{a}\right) \hat{x} + \cos\left(\frac{\pi x}{a}\right) \hat{y} \right] e^{-jk\delta} \quad (11.1)$$

where  $k$  is the free-space wavenumber,  $|x| < a/2$ ,  $|y| < a/2$ , and  $\delta = (x^2 + y^2)/2R_h$ , with  $R_h$  being the slant length of the horn and  $a$  the side of the square aperture. Therefore, for small flare angles, the field structure within the horn aperture is:

$$E_v = \mathbf{E}_A \cdot \mathbf{v} = \frac{E_0}{\sqrt{2}} \left[ \cos\left(\frac{\pi y}{a}\right) + \cos\left(\frac{\pi x}{a}\right) \right] e^{-jk\delta} \quad (11.2)$$

$$E_h = \mathbf{E}_A \cdot \mathbf{h} = \frac{E_0}{\sqrt{2}} \left[ \cos\left(\frac{\pi y}{a}\right) - \cos\left(\frac{\pi x}{a}\right) \right] e^{-jk\delta}$$

such that the E-field vector is parallel to one of the diagonals (Figure 11.3b). One can argue that, strictly speaking, the diagonal horn is not a multimode horn, given that it does not make use of higher-order TE and TM modes. However, it presents the desirable attributes of the usual multimode horns, such as suppressed side-lobes and cross-polarized fields in the E- and H-planes and equal beamwidths in the principal planes. In addition, Johansson [7] showed by using a Gauss-Laguerre expansion of the aperture fields that the diagonal horn pattern couples to the fundamental Gaussian mode with an 84.30% efficiency when  $w_A = 0.43a$ , where  $w_A$  is the beam radius at the horn's aperture. Nonetheless, all the attractive features above are accomplished at the expense of pairs of cross-polarized lobes in the intercardinal planes, making such a horn unattractive for applications where a high level of polarization purity is required. Indeed, the analysis in [7] predicts 10% of the power going into the cross-polarized component. Regarding their fabrication, diagonal horns present a geometry which is suited for being milled onto two symmetric separate pieces (split-blocks), which are then joined. The TE<sub>10</sub> mode losses in the rectangular waveguide are low since the split occurs along the center of the broad walls of the waveguide. Diagonal horns are also easy to pack, which makes them attractive for focal plane imaging applications [7]-[8].

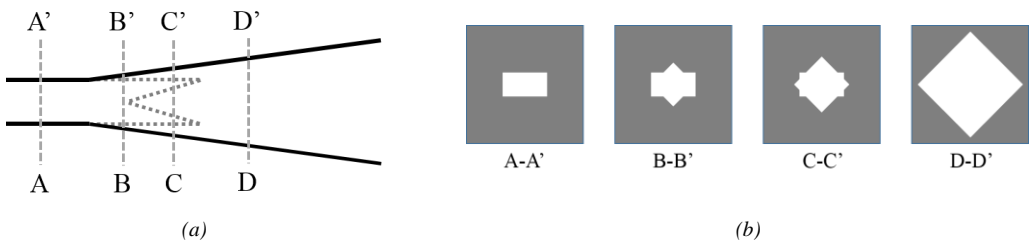


**Figure 11.2.** (a) Longitudinal section of the transition from the rectangular waveguide to the diagonal horn's flared section. (b) Transverse cross-sections through the block at various points along the transition.

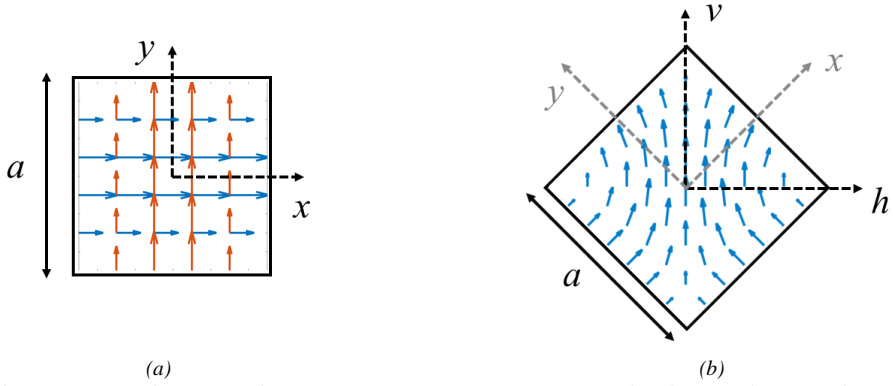


**Figure 11.3.** (a) TE<sub>10</sub> and TE<sub>01</sub> modes coexisting in a square waveguide. (b) Result of combining the two modes in the diagonal horn's aperture.

A second option consists in using multimode axi-symmetric horns. An appropriate combination of the circular TE<sub>11</sub> and TM<sub>11</sub> modes at the horn's aperture leads to far fields with very good beam symmetry and pure linear polarization, as depicted in Figure 11.4. Such a dual-mode horn, also known as Potter horn [9]-[10], consists of a mode converter section, designed to excite the TM<sub>11</sub> mode with a prescribed amplitude, and then a phasing section (the two modes have different cut-off frequencies) to ensure that both modes fulfill the correct relationship at the horn's aperture (see Figure 11.5a). As a consequence of

the required amplitude and phase balance, Potter horns are relatively narrow-band, although they can meet the bandwidth requirements of some applications. Indeed, the Potter horn achieves complete beam-width equalization in all planes, complete phase center coincidence, and at least 30 dB side-lobe suppression in the electric plane over a somewhat narrow band. A similar strategy is used in Pickett-Potter horns [10]-[11], which is a simplification of the Potter design. Essentially, they consist of a smooth-walled conical horn with a single step in the throat (Figure 11.5b). An analysis analogous to the one carried out in [7] to determine the Gaussicity of the pyramidal horn was performed for dual-mode horns in [12]. The fraction of power coupled to the fundamental Gaussian mode is 96.3% when  $w_A = 0.59a$ , with  $a$  being the radius of the horn aperture. This efficiency compares well with the 98.1% of corrugated horns, normally taken as a reference. In addition, only 1.4% of the radiated power goes into cross-polarized fields. Another advantage of Potter and Pickett-Potter horns is that, as in the case of diagonal horns, they are easy to machine using split-blocks.

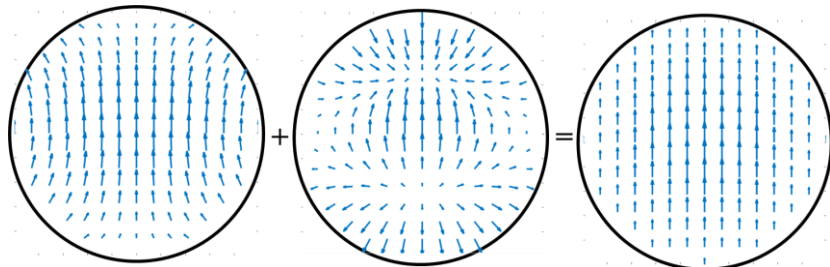


**Figure 11.4.** E-field lines for a  $TE_{11}$  mode and  $TM_{11}$  and how a combination of both in a hybrid mode leads to a very symmetric beam with very pure polarization.

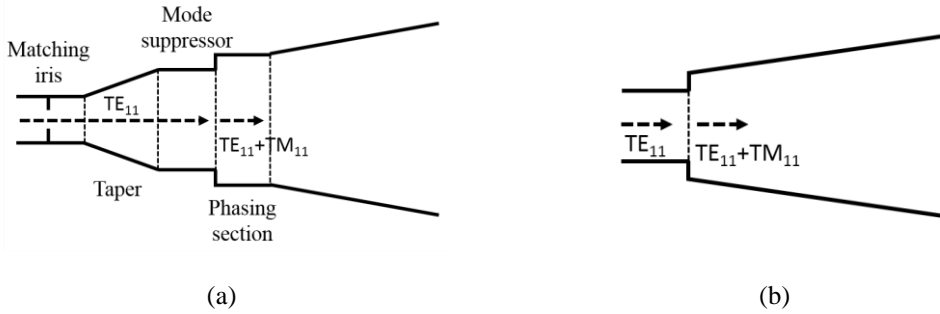


**Figure 11.5.** (a) Cross-section of a Potter horn. (b) Cross-section of a Picket-Potter horn, the  $TM_{11}$  is generated at the step discontinuity.

### 11.2.1. Corrugated horns

In the previous section, we have described two different approaches to generate a hybrid mode at the horn aperture to obtain beam symmetry, low sidelobes, and highly pure linear polarization. Despite the improvement provided with respect to pyramidal and conical horns, the high level of cross-polarized fields that pyramidal horns present in the inter-cardinal planes, and the narrow bandwidth of Potter horns may hinder their use in some applications. The corrugated horn [2]-[3],[13]-[14], also known as scalar horn, is the feed of choice for high-performance systems in which the limitations of diagonal and Potter horns cannot be assumed.

The purpose of the corrugated surface is to provide the means to support the propagation of a hybrid  $HE_{11}$  mode, which results from the combination of the  $TE_{11}$  and  $TM_{11}$  modes. The geometry of a corrugated circular waveguide, including the definition of the different variables, is shown in Figure 11.6 and the general expression of the  $HE_{11}$  mode reads:

$$E_x = A J_0(k_\rho \rho) - B \frac{(X-Y)}{kr_1} J_2(k_\rho \rho) \cos(2\phi) \quad (11.3)$$

$$E_y = B \frac{(X-Y)}{kr_1} J_2(k_\rho \rho) \sin(2\phi)$$

where  $A$  and  $B$  are the amplitude coefficients,  $J_n(k_\rho \rho)$  are the Bessel functions of the first kind and order  $n$ , and  $k$  and  $k_\rho$  are the free space and transverse to  $z$  wavenumbers. Finally,  $X$  and  $Y$  are the normalized reactance and admittance at  $\rho = r_1$  defined as

$$X = -j \frac{Z_\phi}{Z_0} = -j \frac{E_\phi}{H_z} \sqrt{\frac{\epsilon_0}{\mu_0}}; \quad Y = -j \frac{Z_0}{Z_z} = j \frac{H_\phi}{E_z} \sqrt{\frac{\mu_0}{\epsilon_0}} \quad (11.4)$$

One can easily realize from (11.3) that the fields are exclusively polarized in the  $x$  direction when  $(X-Y)=0$ . Moreover, the  $E_x$  component will taper radially with  $\rho$  without any  $\phi$  variation. The  $(X-Y)=0$  condition is usually referred to as balanced hybrid condition and it can be fulfilled either when  $X=Y$  or when both  $X$  and  $Y$  are equal to 0. In a corrugated waveguide, provided that one has several slots per wavelength (preferably four or more),  $E_\phi$  has to vanish at  $\rho=r_1$ , so  $X$  will be 0. In addition, for narrow corrugation ridges ( $t < w/10$ ) and narrow slots ( $w < \lambda/2$ ), the normalized admittance can be approximated as  $Y=1/\tan(2\pi d/\lambda)$  and, it will be thus 0 when  $d=n\lambda/4$ , with  $n$  being an odd integer. In other words, the short-circuit is transformed to an open-circuit at  $\rho=r_1$ , which ensures the absence of axial currents resulting from  $H_\phi$  and implies that  $Y=0$ . In [14] and the references therein, a more refined set of formulas is provided in which  $d$  is modified by a correction factor resulting from a rigorous formulation of the surface reactance. The balanced hybrid condition will be fulfilled only at the frequencies in which  $d=n\lambda/4$ , so the absence of cross-polarization will be determined by the electrical length of  $d$ . Nevertheless, (11.3) shows that the cross-polar term decreases as  $kr_1$  increases and the larger the diameter of the horn, the wider the bandwidth for a given cross-polar level. This is a general property of cylindrical hybrid-mode feeds, where large apertures give an inherently better performance than feeds with a small aperture, although larger apertures will also lead to narrower beam (not suitable for prime feed focus).

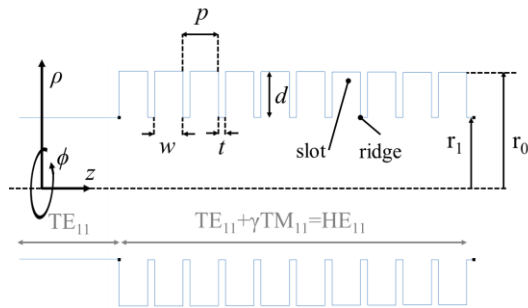


**Figure 11.6.** Corrugated circular waveguide.

We have succinctly explained in the paragraph above how the corrugated surface supports the propagation of the  $HE_{11}$  mode. However, the input of the corrugated horn will typically be the  $TE_{11}$  mode of a circular waveguide. Hence, preceding the flared section of the horn one has to introduce a mode converter to excite the hybrid mode. There are several schemes of mode converter, namely:

- a) variable-depth-slot mode converter [15]-[16], which is the most commonly used mode converter, and provides up to 1.8:1 bandwidths (see Figure 11.7a);
- b) ring-loaded-slot mode converter [17], which provides up to 2.4:1 bandwidths (see Figure 11.7b);
- c) and variable-pitch-to-width-slot mode converter [18], which can deliver up to 2.05:1 bandwidths, although is less commonly used (see Figure 11.7c).

In practice, the number of slots (NMC) in a mode converter is between 5 and 7 for mode converters *a*)

and  $b$ ), and between 7 and 12 for the mode converter  $c$ ).

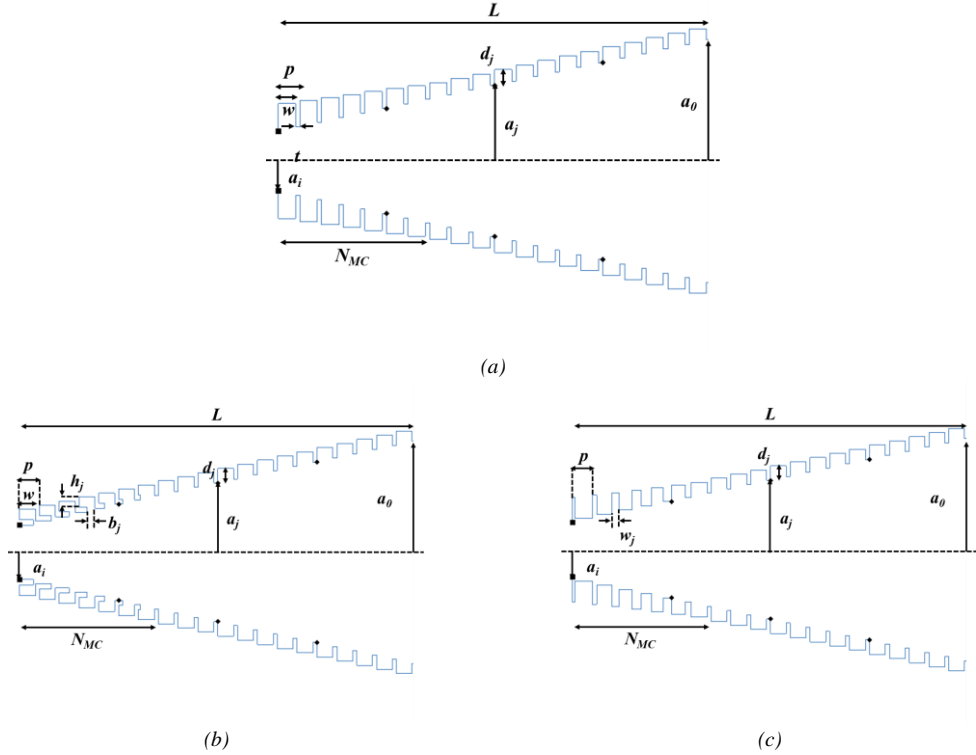


**Figure 11.7.** Conical corrugated horn with: (a) variable-depth-slot mode converter, (b) ring-loaded-slot mode converter and (c) variable-pitch-to-width-slot mode converter.

It is also important to note that corrugated horns are the classical solution for launching Gaussian beams. The optimum Gaussian coupling efficiency of a conical corrugated horn has been studied in [5] and it is equal to 98% when  $w_a = 0.644 a_0$ , where  $w_a$  is the beam radius at the aperture and  $a_0$  is the horn's aperture radius.

Even if conical corrugated horns (Figure 11.7) are the most common option, it is possible to enhance the horn's performance by giving them a profile other than linear [19]. For instance, the authors of [20] proposed a Gaussian profiled horn antenna to improve its electromagnetic performance and/or optimize its geometry (reduce its length, weight, and/or output radius). Similarly, a horn with dual sinus-squared and exponential profile was presented in [21]. On the other hand, Maffei et al. [22] added a flared section at the end of a profiled horn, with the form heuristically developed to give the desired patterns and very low side-lobes. In general, the profile of the horn can be described using combination of exponential, sinusoidal, hyperbolic curves, etc., with control points that are optimized to obtain the desired far-field patterns using non-linear least squares, minmax or genetic algorithms. Figure 11.8a and Figure 11.8b show a corrugated horn with spline profile optimized to have a maximum coupling to the fundamental Gaussian mode (see the magenta line in Figure 11.8d), while keeping a good match ( $S_{11} < 25\text{dB}$ ) across the 490-600 GHz band, as shown in Figure 11.8c. On the other hand, the dual-profile (sine-squared/parallel and hyperbolic tangent/parallel) horns reported in [23] are obtained by exploiting the fact that the coupling from the HE mode in straight corrugated guide to a fundamental Gaussian mode in free space can be improved by exciting higher order HE modes. This analysis, based on higher-order HE modes, provides additional physical insight into the profile choice.

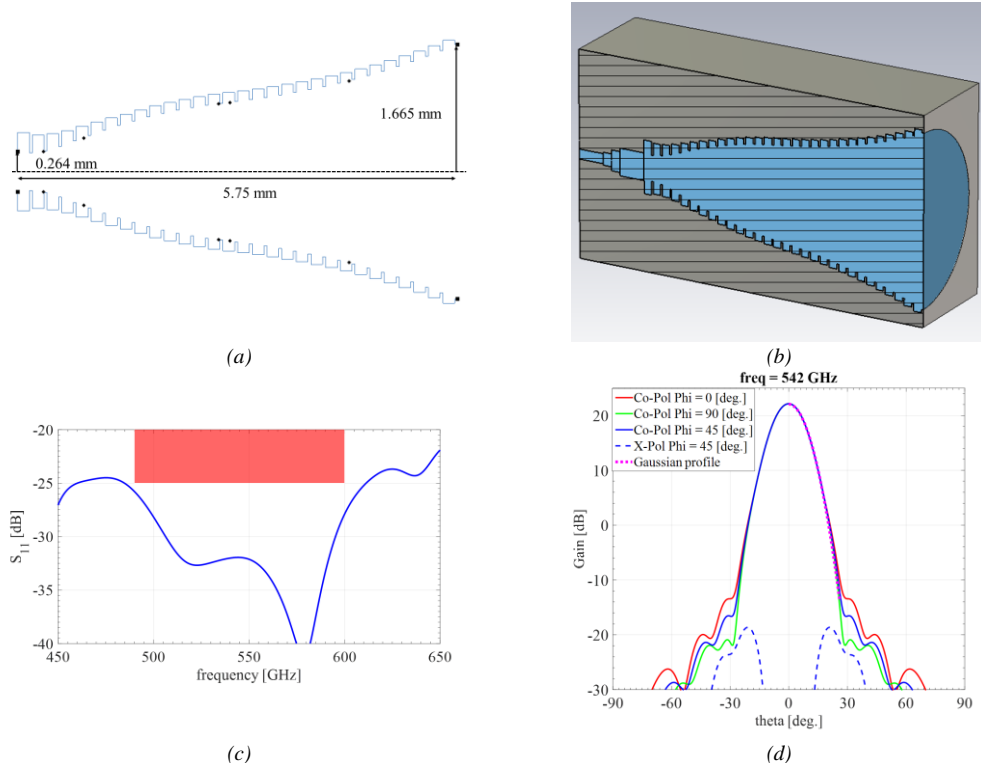


**Figure 11.8.** (a) Spline-profiled corrugated horn. (b) Section of the horn including the rectangular waveguide to circular waveguide transition. (c) Magnitude of the reflection coefficient in dB. (d) Far-field radiation patterns at the central frequency.

A crucial aspect of corrugated horns consists in how to fabricate the narrow ridges at Terahertz frequencies. The continuous evolution of computer numerical control (CNC) milling machines has made it possible to fabricate corrugated horns at millimeter and submillimeter frequencies by direct machining into two halves of a split-block, despite the difficulty of constructing azimuthal corrugations at short wavelengths. However, the length of narrow flare angle feedhorns, and the depth of the matching grooves near the intersection of the circular waveguide and the corrugated conical flared sections restrict the tool clearance available for direct machining operations. Hence, in some cases, a higher cost electroforming process will be required. The first step involves the high precision machining of the internal geometry of the circular waveguide and the corrugated conical section on an aluminum mandrel. The feedhorn is then electroformed by electrochemical deposition of copper and nickel onto the mandrel surface until the desired wall thickness is achieved. Afterward, the mandrel is removed by a chemical etching process. Finishing includes flange soldering and a gold electroplate.

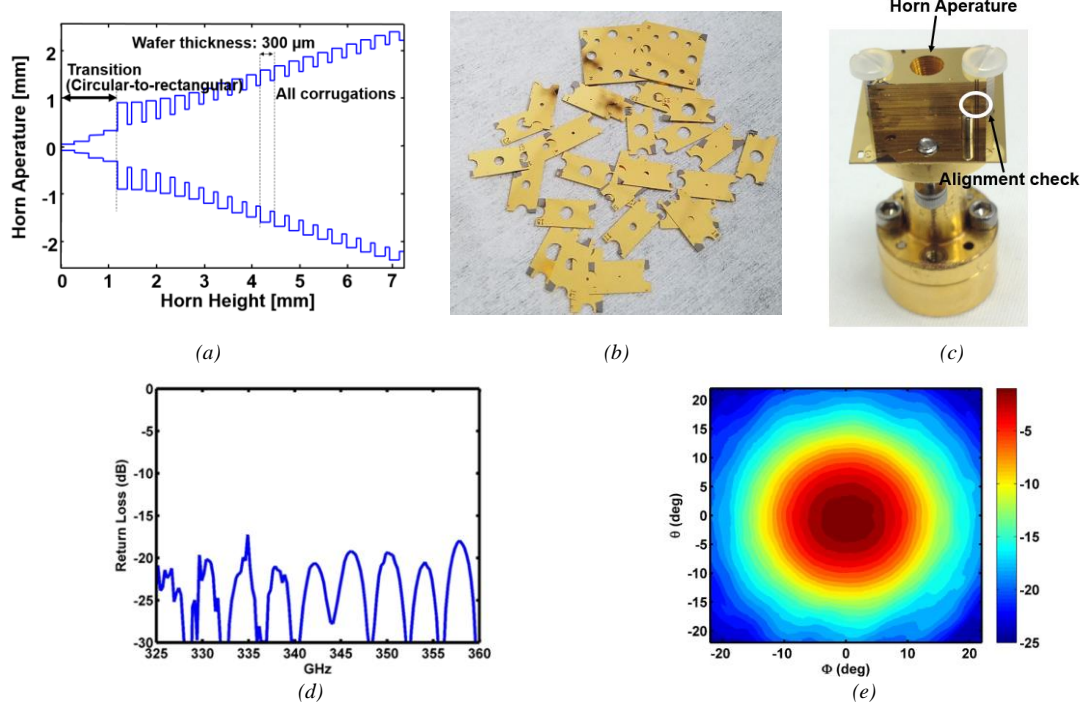
In modern instruments there is a trend towards increasing the number of detectors in the focal-plane, which enables a significant increase in telescopes or imagers mapping speeds. Electroformed horns and machined split-blocks are not easy to adapt to the fabrication of focal planes with a very large pixel count. As an alternative, one can fabricate corrugated horns using platelets [24], which are thin metal sheets [25]-[27] or silicon wafers [28]-[30]. In order to create the corrugations for an array of horns, one has to etch two features in each sheet, namely, through holes of thickness  $p$  and radius  $a_j$ , and cylindrical steps of thickness  $w$  and radius  $a_j+d$ , which serve to create the ridges of the corrugations (see Figure 11.7). These sheets are sandwiched together in a stack of many layers either using screws and pins [25]-[26],[30] or diffusion bonding them together to make a single piece [24]. With the design completed, and the photolithographic masks or machine programs created, many platelets can be reproduced accurately and economically. This technique is estimated to produce good results up to 1 THz.

Figure 11.9a shows the cross section of a platelet conical corrugated horn including a transition, manufactured using a Deep Reactive-Ion Etching (DRIE) process of silicon wafers. The first 20 platelets form a conical corrugated horn. An additional 4 platelets form a circular-to-rectangular waveguide transition connected to the metal waveguide block at WR-2.2 band (330-500GHz). Regarding

microfabrication, it requires only two etch depths of 100 and 200  $\mu\text{m}$  from the front- and back-side of a 300  $\mu\text{m}$  thick wafer, respectively. During the etching processes of 100/200  $\mu\text{m}$ , screw holes, trenches for the alignment compression pins, and alignment marks all etched are simultaneously. A rectangular to circular waveguide transition is made on a separate 4-inch silicon wafer. All 24 silicon platelets are then coated with 2  $\mu\text{m}$ -thick gold using a metal sputtering system. Finally, the 24 gold-coated silicon platelets are precisely aligned and stacked together using a silicon compression pin technique [31].

The horn presents a return loss around 20 dB across the band (see Figure 11.9c), better than 30 dB cross-polarization, and more than 20 dBi directivity over a 20% fractional bandwidth at 340 GHz. The measured radiation pattern also presents a good beam symmetry, as shown in Figure 11.9d.

To conclude this section, it is worth mentioning the importance that 3D printing techniques might have in the future development of large focal plane arrays of corrugated horns. In [27],[28], the capability of fabricating W-band corrugated horns has been investigated.



**Figure 11.9.** (a) Detail of the 20 corrugations in the conical horn. (b) Different 300  $\mu\text{m}$ -thick silicon wafers before assembly. (c) Picture of the fabricated and assembled platelet antenna consisting of 24 300  $\mu\text{m}$ -thick silicon wafers. Apart from the silicon compression pins (not visible in the picture), two plastic screws and dowels pins were included for alignment. (d) Measured magnitude of the reflection coefficient in dB. (e) Measured co-polar radiation pattern at 330 GHz, normalized to the maximum directivity value (21.2 dB).

Summarizing, corrugated horn antennas provide low cross-polarization, excellent beam-circularity, low side-lobe levels, nearly constant beam-width over a large frequency band, low loss, high Gaussian coupling efficiency, and low VSWR. However, at millimeter and sub-millimeter-wave frequencies, the decreasing horn size results in increasing manufacturing difficulties, time, and cost. Therefore, corrugated horns are hardly compatible with multi-pixel arrays. We have discussed the design, fabrication and assembly of platelet corrugated horns and focal plane arrays, which provide good performance and constitute a cost-effective alternative to electroformed corrugated horns. However, these techniques have their own limitations. In the case of platelet horns, the maximum wafer thickness has to be of the order of  $\lambda/4$  to maintain the hybrid boundary condition on the horn's wall. Therefore, long horns (necessary for large  $f/D$ , which stands for the focal distance  $f$  over the reflector diameter  $D$ ) will require stacking a large number of wafers, which complicates their assembly. Therefore, solutions such as multi-flared angle [32]-[34] and spline-profiled horns [35] have been extensively explored.

### 11.2.2. Multi-flare angle

Multi-flare horns are a multi-mode horn consisting of a small number of sections (i.e. typically 2 to 3) with a linear profile. The simple interior profile of makes them much easier to fabricate than spline, diagonal, Potter, and corrugated horns because it enables a direct-drilling technique that avoids electroforming and split-block designs. As a result, multi-flare angle horns have been identified as promising solutions allowing fabricating large arrays out of a single metal block [32]-[33].

The fabrication steps are straightforward:

- 1) A machine tool is fabricated. Its cutting edges are manufactured with the shape of the optimized horn's interior.
- 2) The horns are drilled out of a metal block one at a time.
- 3) For a better surface accuracy, the input waveguide is machined after the horn steps are drilled.

This approach then shifts the challenge from fabrication to optimization, but by using genetic algorithm optimization excellent designs have been achieved. Depending on the application, horn performance requirements are set in terms of gain, beam-width, side lobe level, cross-polarization, beam-efficiency, and return loss. The feed needs to comply with a f-number ( $f/D$ ) for a given edge taper. The directivity  $D_0$  of a horn can be determined for a given f-number using [5]:

$$D_0 = \frac{8\pi^2 w_{0,feed}^2}{\lambda^2} \quad (11.5)$$

where  $w_{0,feed}$  is the beam waist radius of the feed given by:

$$w_{0,feed} = 0.216 \cdot [Te(dB)]^{0.5} \frac{f}{D} \lambda \quad (11.6)$$

where  $f$  is the focal length, and  $D$  is the reflector diameter.

It is necessary to optimize a horn accurately based on the aforementioned requirement over a given frequency range. We will illustrate the optimization of four multi-flare angle horns as summarized in Table 11.1.

**Table 11.1. Optimized multi-flare angle horn**

	Frequency band (GHz)	Bandwidth (%)	$f / D$	Edge taper (dB)	Directivity (dBi)
Horn #1	1700-2100	21	6	-10	31.2
Horn #2	118-183	43	2.1	-12	22.1
Horn #3	230-390	52	2.1	-12	22.1
Horn #4	650-690	6	2.97	-12	25.9

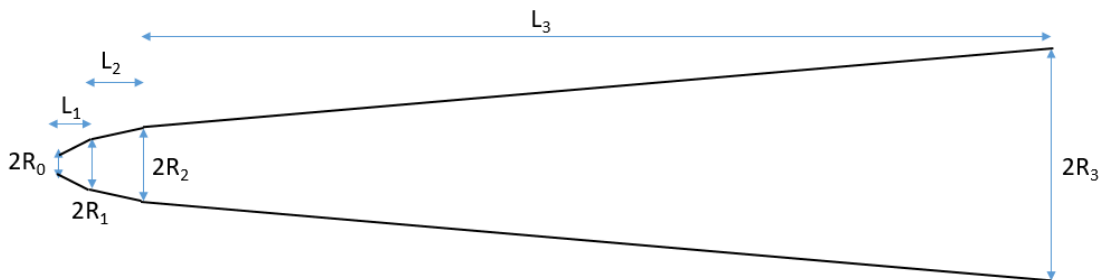


**Figure 11.10. Multi-flare angle horn with three sections.**

#### 11.2.2.1. Optimization method

The multi-flare horn antennas are optimized using an in-house BoR-FDTD (Body-of-Revolution FDTD) solver combined with real-valued and binary-coded genetic algorithm (GA) [38]. A detailed description of the BoR-FDTD technique can be found in [38]-[40]. The employed GA is associated to linear-combination selection, crossover, and mutation operator of the chromosomes [41]. The CAD tool is a combination between a time domain full-wave analysis solver (BoR-FDTD) and the global search algorithm (GA). This CAD tool is designed to find the global optimum complying with the desired specifications in radiation (i.e. directivity, cross-polarization, and beam circularity) and return loss over

a specified frequency band. It is based on a time domain solver (FDTD) where one simulation can cover the entire frequency range. Indeed, this can be done using Fourier transform of the time domain signal. This makes the tool very useful where such large frequency band needs to be analyzed.

To reduce the computation time during the optimization process, the typical FDTD mesh size is  $\Delta\rho = \Delta z = \lambda_0/20$ , where  $\lambda_0$  is the free space wavelength. To check the validity of the staircase approximation, the numerical result is checked with finer mesh ( $\Delta\rho = \Delta z = \lambda_0/50$ ) after the optimization is completed.

The optimization accounts for the cross-polarization, the antenna directivity, and beam circularity. In addition, this optimization is effected for multiple frequency points ranging from the minimum frequency  $f_{\min}$  to the maximum frequency  $f_{\max}$ . Hence, we chose a cost function that is minimized during the optimization process for horns having a given directivity  $D_0$ , low cross-polarization level (i.e. X-pol < -20dB), high beam circularity, and a maximum length  $L_{\max}$  (i.e.  $L_1 + L_2 + L_3 \leq L_{\max}$ ). The cost function is given as:

$$Fitness = \sum_{f=f_{\min}}^{f_{\max}} \sum_{i=1}^N \sum_{j=1}^M W(f) \Delta(\theta_i, \phi_j) \quad (11.7)$$

where:

$$\Delta(\theta_i, \phi_j) = \begin{cases} M_{Low} - G & (\text{if } G < M_{Low}) \\ 0 & (\text{if } M_{Low} \leq G \leq M_{Up}) \\ G - M_{Up} & (\text{if } G > M_{Up}) \end{cases} \quad (11.8)$$

$$W(f) = 1, \forall f : f_{\min} \leq f \leq f_{\max} \quad (11.9)$$

In this relation,  $G(\theta_i, \phi_j)$  is the horn antenna radiation pattern, and  $M_{Low}(\theta_i, \phi_j)$  and  $M_{Up}(\theta_i, \phi_j)$  are the desired masks of the pattern models.  $N$  and  $M$  denote the number of observation points in  $\theta$  and  $\phi$  directions of the 3D patterns. In this work  $N, M, \theta_i$  and  $\phi_i$  equal 361, 3,  $[0:0.25:90]^\circ$  and  $[0:45:90]^\circ$ , respectively. The function  $\Delta(\theta_i, \phi_j)$  measures the differences between the horn radiation pattern  $G(\theta_i, \phi_j)$  and the lower mask  $M_{Low}(\theta_i, \phi_j)$  and the upper mask  $M_{Up}(\theta_i, \phi_j)$  (11.8). The fitness function is pre-coded to include the weighting control  $W(f)$  for stressing on the optimizing frequency. In this case, all the frequencies have the same weight, and therefore the weight coefficients are assigned to 1 (11.9).

To control the cross-polarization level and the maximum length value of the horn antenna, we use the penalty technique as demonstrated in [38]:

- if the cross-polarization level > -20dB is detected, the cost function will be double ( $Fitness = Fitness \times 2$ ),
- if the total length of the horn is bigger the maximum length  $L_1 + L_2 + L_3 \geq L_{\max}$ , the cost function will be triple ( $Fitness = Fitness \times 3$ ).

The input waveguide radius  $R_0$  is fixed and its value is determined to provide a good starting point for obtaining a good return loss, with TE<sub>11</sub> well above the cut-off frequency and TM<sub>11</sub> below the cut-off frequency at the design frequency. As such antennas are optimized by combining the TE<sub>11</sub> mode with a TM<sub>11</sub> mode, it is important to make sure no TM<sub>11</sub> mode can propagate through the input port. Otherwise, a degenerative TM<sub>11</sub> mode could affect the radiation pattern of the antenna. The value  $R_3$  is approximated using a closed-form equation for a standard linear horn providing a directivity  $D_0$ . The parameters  $R_1$ ,  $R_2$ ,  $L_1$ ,  $L_2$ , and  $L_3$  are then optimized.

#### 11.2.2.2. 1900 GHz multi-flare angle horn antenna

##### Design optimization

A feed horn with a f-number f/D of 6 is designed within the 1700-2100GHz frequency band. An f/D of 6 translates into a gain of 31.2 dBi for an edge taper Te[-10dB] (see Eq. 11.5 and 11.6). The optimized horn has a gain of 31.2 dBi at 1900 GHz with a total length of 9.45 mm. Its cross-polarization is under -22 dB and its gaussicity higher than 97% within the 1700-2100 GHz frequency range. The optimized dimensions are summarized in Table 11.2.

The radiation patterns obtained using the BoR-FDTD code are shown in Figure 11.11 at 1700 GHz and 2100 GHz in the *E*-, *D*-, and *H*-plane. The cross-polarization level remains below -22 dB across the frequency range and a good beam-circularity is obtained.

**Table 11.2.** Optimized dimensions in micrometer for the 1.9THz multi-flare angle horn

	$R_0$	$R_1$	$R_2$	$R_3$	$L_1$	$L_2$	$L_3$
Optimized	74	189	261	1279	237	237	8976
Measured	83	185	253	1262	231	226	8867

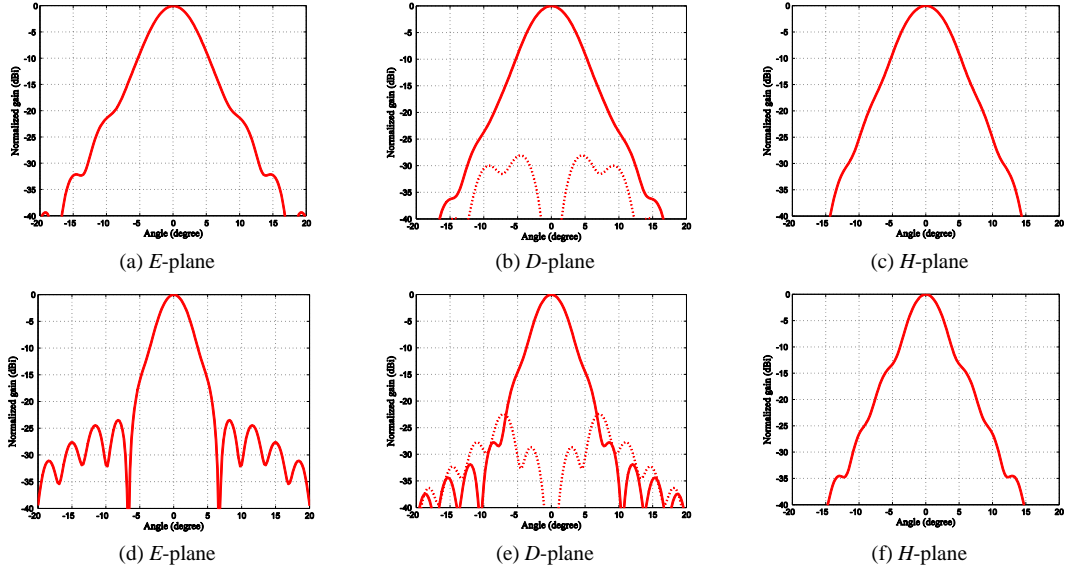


**Figure 11.11.** Calculated radiation patterns with IETR BoR-FDTD at (top) 1700 GHz and (bottom) 2100 GHz.

### Fabrication

The multi-flare angle horn antenna is machined out of a single metallic block of oxygen-free copper (Figure 11.12) using an end-mill that is shaped in accordance with the multi-flare angle horn contour. The fabricated multi-flare angle horn antenna is shown in Figure 11.12. Four horns were manufactured and one was cut in half for dimension inspection (Figure 11.12). The designed and measured dimensions are compared in Table 11.2. The measured dimensions are all within 5% of the design except the throat radius. A better alignment of the input waveguide to the horn was obtained when the circular input waveguide was milled through the aperture of the horn, compared to attempting to mill from the backside. However, doing so requires an extremely high aspect ratio end-mill to reach down the horn. Hence, the tool tends to bow as it cuts and produced a wider throat.

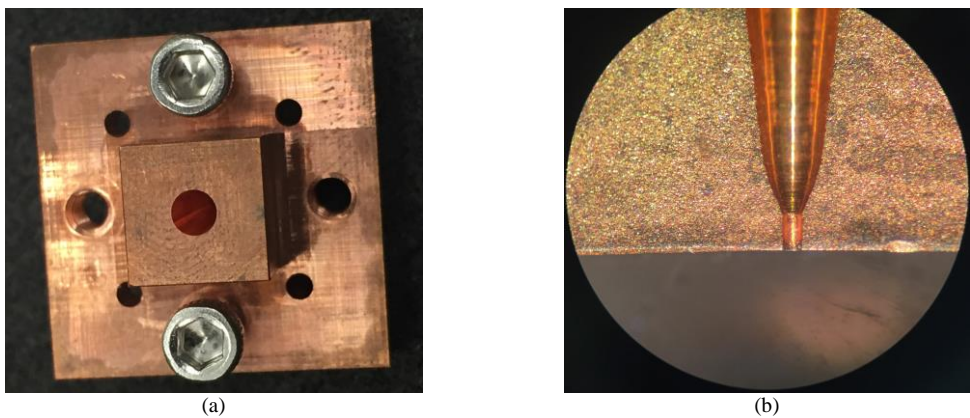


**Figure 11.12.** Fabricated 1.9 THz multi-flare angle horn prototype. (a) Antenna prototype. (b) Cross-section of the antenna prototype.

### Measurement

The multi-flare angle horn is measured in transmission mode with an Infrared Labs HLR-5 bolometer

(Figure 11.13). A 1.9 THz multiplier chain consisting of a Millitech WR-10 AMC, a JPL GaAs WR-10 power amplifier chain, a JPL designed doubler and two JPL triplers are assembled to drive the horn [33]. The output of the 1.9 THz tripler includes a rectangular to circular transition. The output power at the circular waveguide that feeds the horn is approximately 600 nW. The bolometer is a cryogenically cooled silicon bolometer with a responsivity of 220000 V/W focused by a Winston cone with an  $f/D$  of 3.8. The bolometer is insensitive to polarization so a grating is used to filter either the co- or cross-polarization. The multiplier chain is mounted on a stepper-motor controlled mount that rotates in two axes around the approximate phase center of the horn. The synthesizer driving the multiplier chain is cycled at 50 Hz and a lock-in amplifier (SR-830) is used to detect the measured power. Finally, a computer is used to record the output signal from the lock-in with the stage's position.

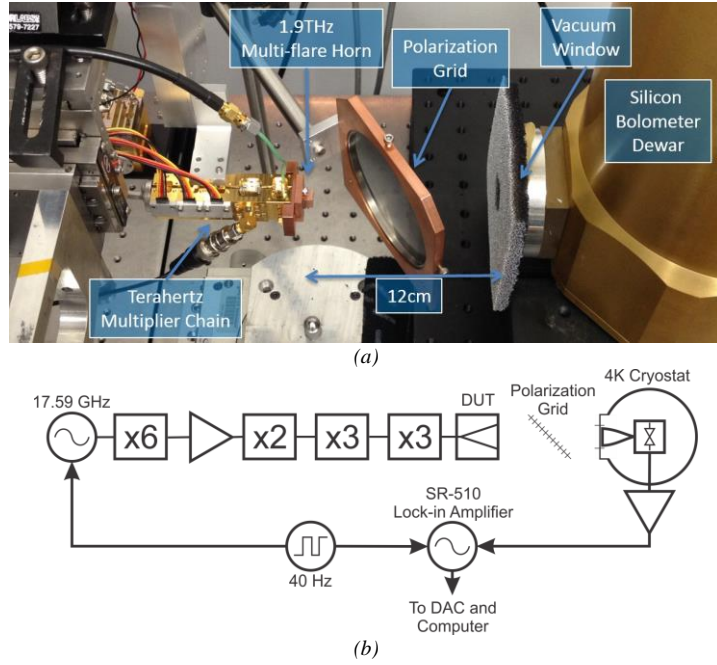


**Figure 11.13.** Radiation pattern measurement set-up using an Infrared Labs HLR-5 bolometer. (a) Photograph and (b) block diagram of the measurement set-up.

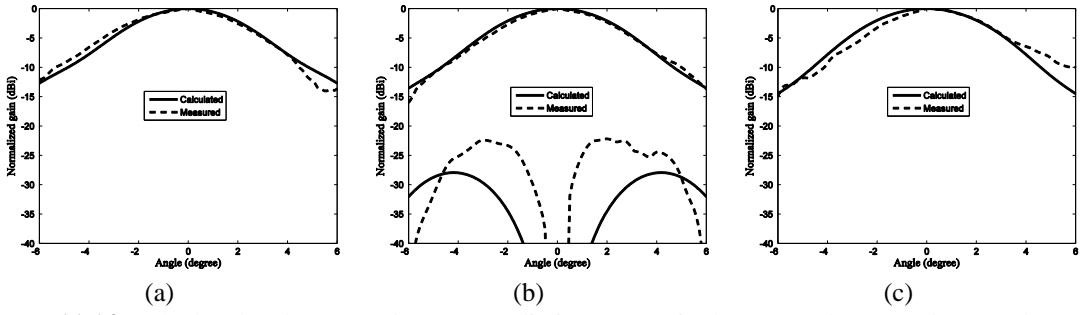


**Figure 11.14.** Calculated and measured antenna radiation pattern in the (a)  $E$ -, (b)  $D$ -, and (c)  $H$ -planes.

The radiation pattern is measured at 1.9 THz in the  $E$ -,  $D$ -, and  $H$ -planes. The calculated and measured results shown in Figure 11.14 are in good agreement. The directivity is calculated from the normalized intensity measured over a  $\pm 6$ -degree scan in both elevation and azimuth. The measured directivity of 31.7 dBi is very close to the design value of 31.6 dBi. To demonstrate the fabrication yield, the three fabricated horns are measured and only 0.1 dB variation in gain is observed. The measured cross-polarization remains below -20dB. Using the Friis formula, the horn efficiency is assessed to be around  $80 \pm 15\%$  [33].

#### 11.2.2.2. TWICE multi-flare angle horn antenna

Three multi-flare angle horns are designed for the mission Tropospheric Water and Cloud ICE (TWICE) which consists of a radiometer integrated in a 6U CubeSat measuring water vapor and ice clouds in upper troposphere. First, the 183 GHz channel and 380 GHz channels are chosen to retrieve water vapor in the troposphere and upper troposphere / lower stratosphere (UTLS). To constrain the water vapor retrievals, 118 GHz channel measures tropospheric temperature profile using O<sub>2</sub> absorption line.

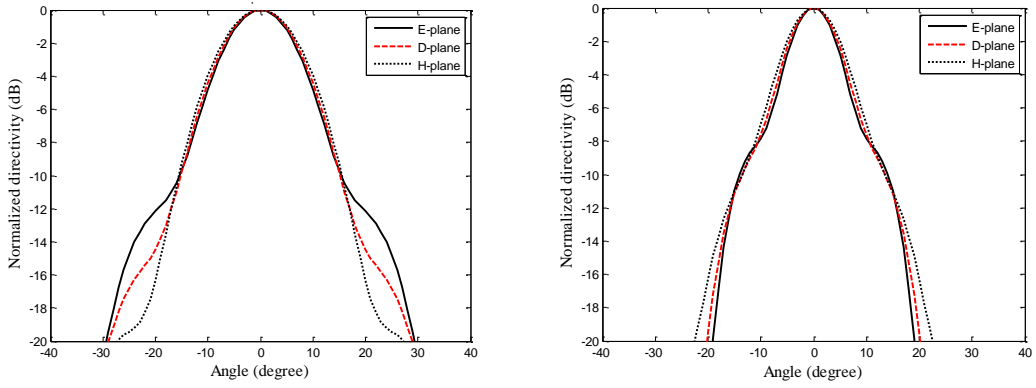
Horn #2 and #3 are optimized across broad frequency bands (i.e. bandwidth > 40%) and horn #4 is optimized across a narrow frequency band (i.e. bandwidth = 6%) (Table 11.1). The optimized dimensions for each antenna are summarized in Table 11.3. The optimized radiation pattern for each antenna is shown in Figure 11.15 at the lower and upper band-edge frequencies. The multi-flare angle horn antennas clearly demonstrate low cross-polarization levels (i.e. <-19 dB), high beam circularity, and high Gaussicity.

**Table 11.3.** Optimized dimensions in millimeter for TWICE's multi-flare angle horns

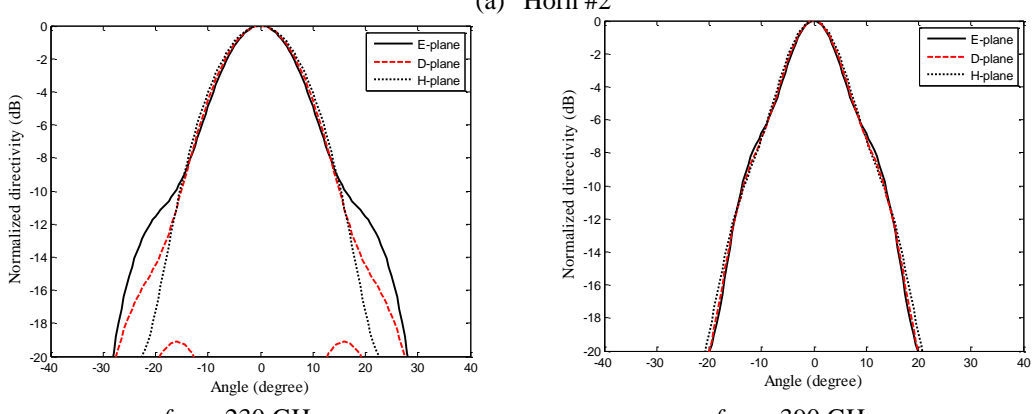
	$R_0$	$R_1$	$R_2$	$R_3$	$L_1$	$L_2$	$L_3$
Horn #2	0.900	1.995	2.518	5.500	6	8.911	11.608
Horn #3	0.450	0.884	1.211	2.746	4.339	4.777	6.141
Horn #4	0.230	0.496	0.613	2.004	0.492	1.346	6.506

As this specific mission uses single feed elements, the feed horns are machined by milling machines, operated under computer numerical control (CNC) and using a split block package (Figure 11.16). This allows to integrate the rectangular-to-circular waveguide transition in the same block.

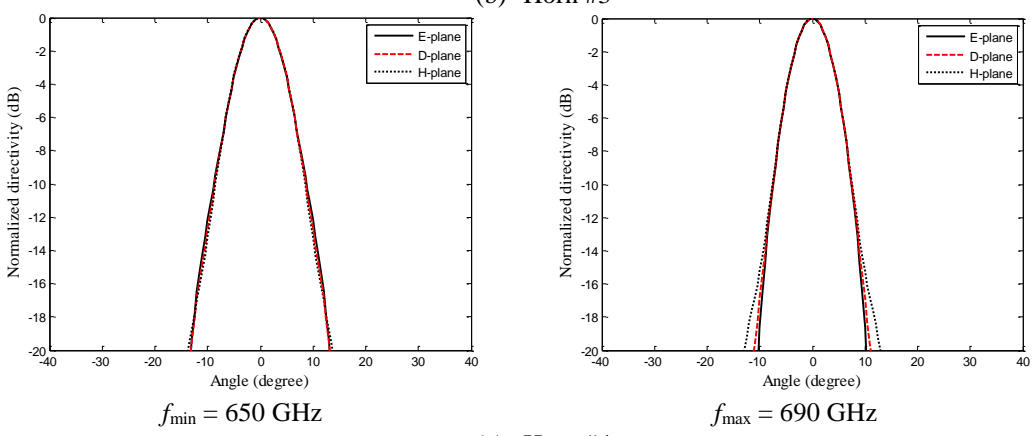
Horn #4 was fabricated and measured. The calculated and measured radiation patterns at 670 GHz (Figure 11.17) are in excellent agreement.



(a) Horn #2



(b) Horn #3



(c) Horn #4

**Figure 11.15.** Optimized radiation patterns of each horn.

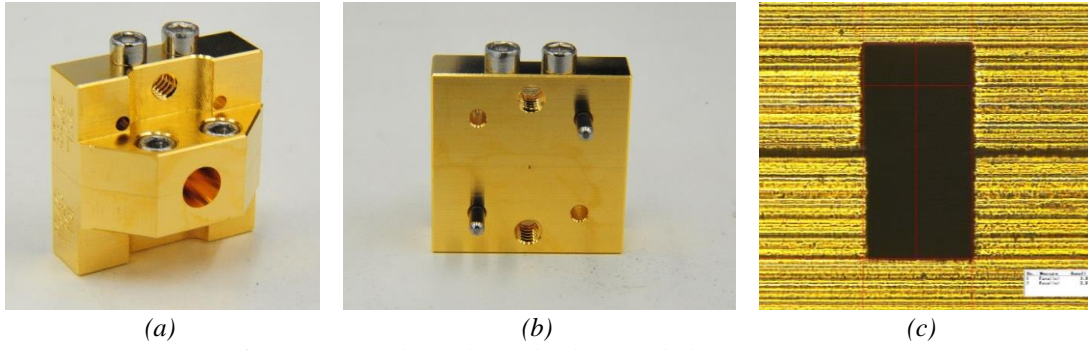


**Figure 11.16.** Channel 3 multi-flare angle horn for TWICE.

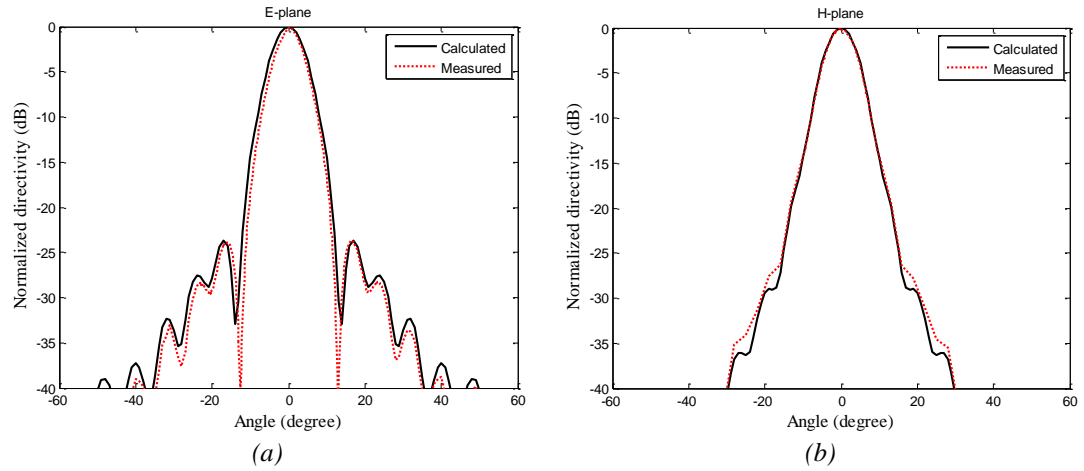


**Figure 11.17.** Calculated and measured radiation pattern of the channel 3 multi-flare angle horn at 670GHz.

### 11.2.3. Smooth-walled horn

It is also possible to define the profile of our axisymmetric horn using cubic splines and then optimize the horn by shaping the splines. Such spline profile is typically described using a few nodes (two extreme nodes and five inner nodes, as shown in Figure 11.18, in order to simplify the optimization process by limiting the number of parameters. The electromagnetic parameters of the horn are evaluated using modal matching techniques [3] or body of revolution solvers [38]-[41] at each optimization step. The initial value of the parameters  $d_1 \dots d_6$  and  $L_1 \dots L_6$  are introduced by the user, and they can be retrieved from the radius and length of a corrugated horn with the desired beam waist, bearing in mind that spline-profiled horns are, in general, longer. An alternative starting profile is given by a  $\sin^{0.75}$  profile followed by a Gaussian section. Then, the parameters are optimized to provide the desire radiation pattern by minimizing a penalty function. The penalty function used is analogous to the one described in the previous section. Finally, it is important to note that some constraints must be applied to the radii to force the optimizer to create shapes that are physically possible to manufacture.

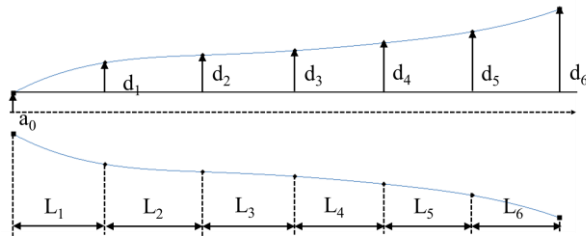


**Figure 11.18.** Example of spline-profiled smooth-walled horn, including the variables used to define the cubic splines nodes.

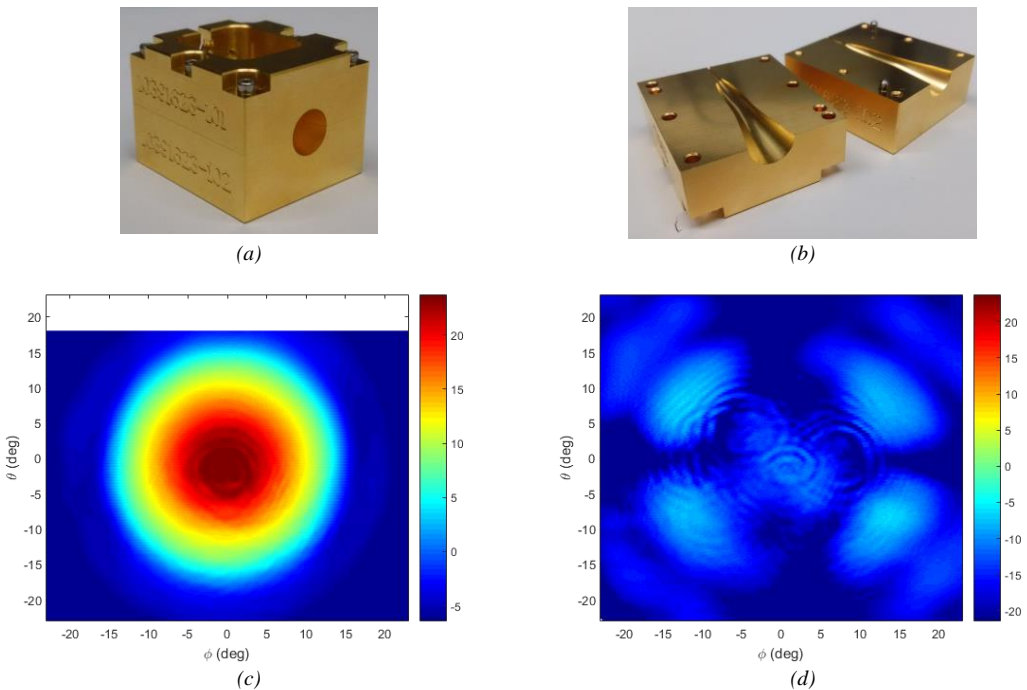


**Figure 11.19.** (a) Block with a spline-profiled horn. (b) Split-blocks.

Figure 11.19a shows a block with a spline-profiled horn, whereas in Figure 11.19b one can see the two split-blocks and, in the right-hand side block, one can also distinguish the dowel pins used for alignment. The horn has been designed for the 300-380 GHz band, where the simulated magnitude of the reflection coefficient is lower than -30 dB. Figure 11.19c shows the measured co-polar directivity pattern at the central frequency, while Figure 11.19d shows the cross-polar one. The measured directivity

is 24.25 dB. The ripples in the main lobe are due diffraction and standing wave effects in the measurement set-up. In this particular design, beam symmetry and cross-polar discrimination have been slightly sacrificed in order to obtain a good impedance matching over a larger frequency band.

## 11.3. Lens antennas

### 11.3.1. Introduction and State of the Art

As it has been explained in the previous section, horn antenna can be fabricated either by split block machining, drilling a metal block with custom drill tips or stacking layers of etched holes in silicon to form platelet horns. Although these techniques can provide good efficiencies at terahertz, higher directivities are difficult to achieve. The higher the directivity the longer the horn, which increases the conductor losses and the fabrication tolerances. Thus, lenses may be preferred at submillimeter-wave frequencies; they can be fabricated with silicon micro-machining and be easily integrated with the front end.

Dielectric lens antennas are taken from the optical regime, replacing the waveguide horn for a planar printed antenna on a thick dielectric and a silicon lens [42]. The advantages of these hybrid antennas compared to waveguide systems are clear: low loss, easy integration and low cost of manufacture, as the antennas can be fabricated using photolithographic techniques and the lenses using laser micromachining. They are commonly found in focal plane array configurations for imaging applications as in [43],[44], providing high efficiency over a narrow bandwidth with double slots antennas. They can also be used as standalone antennas using broadband printed antenna such as bow-ties, logarithmic spirals as photo-mixing antennas for spectroscopy applications as in [45]-[49].

The use of a dielectric lens is the most practical solution for obtaining high efficiency from a planar antenna at terahertz frequencies. When planar antennas are printed on dielectric substrates, they are prone to suffer from power loss due to the surface wave modes propagating within the substrate. These surface waves are confined inside the dielectric (they have a propagation constant larger compared to the free space) and absorb a certain percentage of the radiated power, which constitutes an efficiency loss. If the planar antenna is printed on the back of a high dielectric lens, the radiation will mostly go to the highest dielectric and by the use of a lens profile this radiation will be released into free space. This solution has been extensively used in the literature because of its simplicity and mechanical robustness compared to the use of substrate membranes, which should be in the order of  $0.04\lambda_0$  or  $0.01\lambda_0$  for a low-loss operation of an elemental slot or a dipole antenna, respectively [43].

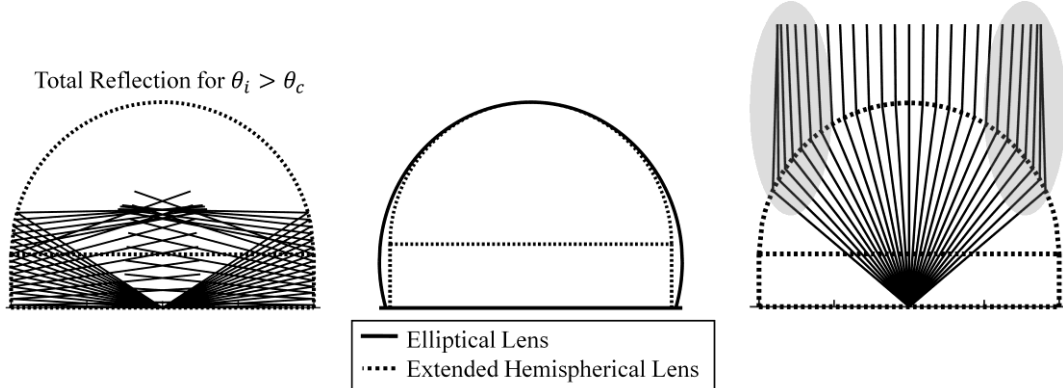


**Figure 11.20.** Lens illumination scheme representing the reflection losses, loss in Gaussicity and phase error of extended hemispherical dielectric lenses.

The dielectric lens design that has been most extensively is the extended hemispherical lens proposed by Rutledge [52]. The extended hemispherical shape is synthetized from an ellipsoidal shape where the antenna feed is placed at the second focus  $F$  of the ellipse with an eccentricity  $e = 1/\sqrt{\epsilon_r}$  in order to achieve maximum directivity and provide good coupling to an optical system. The rays emerging from the focus point above the critical angle will radiate outside the lens and will be perfectly collimated, while the rays that hit below will be reflected in different directions. The performance is constrained by three effects, all caused by the illumination of the lower part of the lens. The first is the dispersion effect caused by the multiple reflections that the rays undergo when illuminating the lower portion of the lens, even with the use of a matching layer (see Figure 11.20a). The second is the phase error associated to the

difference between an ideal elliptical and an extended hemispherical lens (see Figure 11.20b). The last is the coupling loss to the optical system, i.e. how good the antenna is coupled to a Gaussian beam, defined as Gaussicity (see Figure 11.20c). Thus, to improve the performance of these lens antennas the solution has been to employ directive feeds which focus the radiation on the upper part of the lens. That is why double slots, which avoid the illumination of these areas, are preferred as lens antenna feed compared to a simple dipole or slot [44].

A solution for this limitation was recently presented in [53] and [54]. It consists of the combination of these simple printed antennas with a leaky wave cavity between the lens and the feed antenna. This section will be centered on the use of a leaky wave mechanism for a waveguide type of antenna feed. It is a work that was first started on [55] and has been continued on [56] and [57]. The general design rules and the fabrication will be covered in this chapter, with a focus on the development and challenges for these dielectric lens waveguide antennas.

### 11.3.2. Silicon Micro-Lens Antennas Fed by Leaky-Wave Waveguide Feeds

From the guidelines of Jackson [58], Neto et al. proposed in [59] and then in [53] and [54] the use of leaky wave cavities to increase the gain of planar printed antennas at terahertz frequencies. The cavity increases the directivity of the antenna feed that excites the dielectric lens in order to diminish the impact of the reflections at the dielectric air interface.

Instead of using resonant dielectric layer stratifications as in [60], the lens can be considered an infinite layer of dielectric. By leaving a gap between the antenna feed and the lens, the directivity of the feed increases. The highest directivity is achieved at broadside when the cavity thickness is  $\lambda_0/2$ , being  $\lambda_0$  the wavelength in the air, which leads to a resonance at  $f_0$ . There are three modes propagating in the cavity: the dominant  $TE_1$  and  $TM_1$  modes that point towards broadside, and the non-desired  $TM_0$  mode that radiates towards larger angles. The radiation of the  $TM_0$  mode will not be intercepted by the lens, resulting in a spill-over loss. The spillover loss of the lens is defined as the amount of power transmitted that is not caught by the aperture of the lens.

For the correct excitation of the leaky wave modes using a waveguide as a feeding structure, a membrane with a double arc slot iris is required. The pair of slots are excited in phase and are separated by a distance such that their contributions cancel each other. This double slot iris configuration cancels the spurious mode  $TM_0$  mode generated inside the leaky wave cavity [61]. By adjusting the length and the width of the slot, the antenna impedance is matched to the  $TE_{10}$  mode of the waveguide. An example of a design is shown in Figure 11.21b, where two double slots are tuned to operate 550GHz on a 15% bandwidth for the dimensions specified. Dual polarization can be achieved if another set another pair of arc slots are placed orthogonally from the original (see the inset of Figure 11.21a) and excite the waveguide feed with two linear  $TE_{10}$  modes.

Using the dimensions of the provided example we can examine the radiation patterns along the infinite silicon dielectric. An example of such patterns for the leaky wave feed designed at 550 GHz is shown in Figure 11.22a and Figure 11.22b. As it can be seen, the peak directivity in the broadside direction and the radiation patterns are very symmetric. This pattern makes it very suitable to feed a focusing element such as a lens with a moderate f-number (F/D). Due to the high directivity of the feed, the lens surface can be in the near or far field of the antenna, depending on the lens aperture one needs to use. An example is shown in Figure 11.22b, which illustrates that broader patterns are achieved in the case of the operation in the near-field compared to the far-field patterns. Thus, special care needs to be taken into account when optimizing the lens antenna.

The phase center for the leaky wave is not in the plane of the waveguide aperture, it is below the waveguide aperture. This is clearly perceived in the phase of the radiation patterns shown in Figure 11.22 example, which have been calculated considering the reference plane is at the ground plane of the waveguide feed. This displacement of the phase center from the waveguide feed can be compensated by adjusting the height of the lens, as it will be shown next.

The lens geometry, shown in Figure 11.23a is characterized by a silicon wafer of thickness  $W$  on top of the cavity and a silicon lens defined by a certain diameter  $D$ , edge angle  $\theta_s$ , radius of the hemisphere  $R$  and height of the lens  $H$ . All these parameters need to be optimized to achieve maximum gain and Gaussicity.

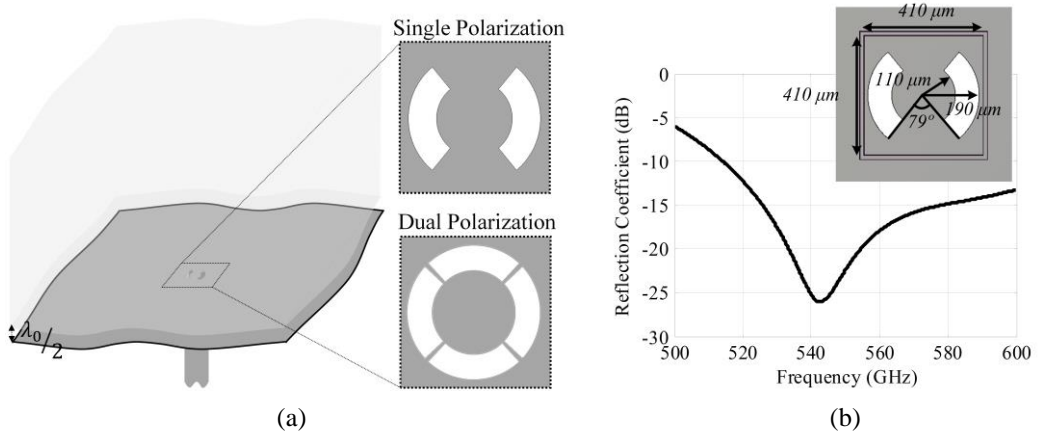


**Figure 11.21.** (a) Scheme of the leaky wave waveguide feed and an inset of the iris for single polarization (up) and for double polarization (down). (b) Reflection coefficient example at 550GHz for the dimensions shown in the inset. The air cavity has a thickness of  $273\mu\text{m}$  and the membrane is  $15\mu\text{m}$  thick.

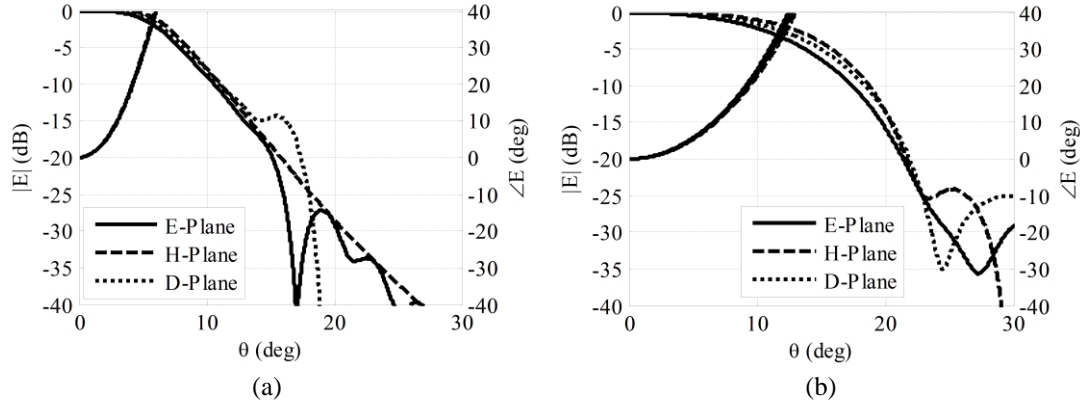


**Figure 11.22.** Directivity (right axis) and phase (left axis) of the leaky wave waveguide feed inside the silicon, (a) at the far field and (b) at the near field distance of  $4.5\lambda_0$ .

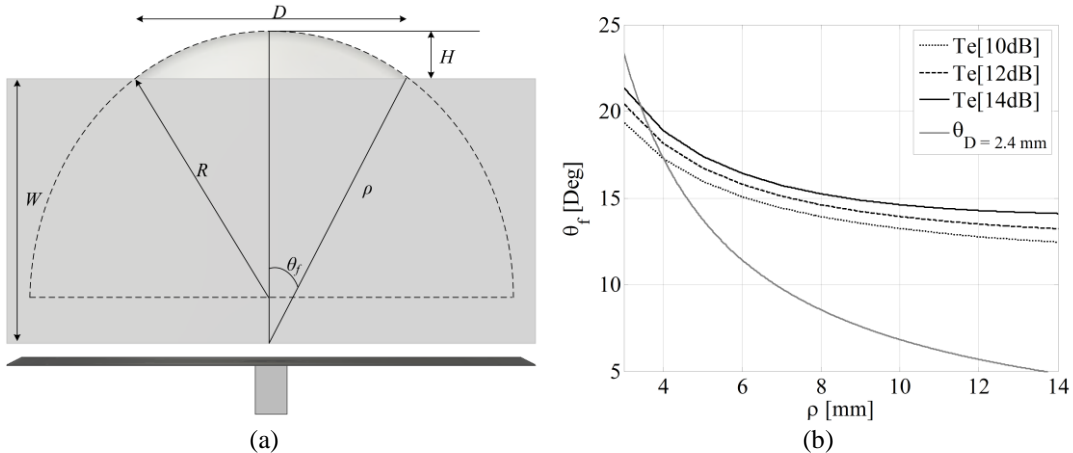


**Figure 11.23.** (a) Sketch of the silicon micro-lens geometry. (b) Example that illustrates the relationship between the taper angle  $\theta_f$  and the wafer thickness  $W$  at 550 GHz.

In order to do the optimization of the antenna and lens, a Physical Optical (PO) tool is essential to decrease the computational time that a full-3D electromagnetic simulator would need to compute and optimize the whole structure. For all the optimizations, a combination of a full 3D simulation and a PO

tool have been employed. The full 3D simulator provides accuracy in the computation of the primary field of the feed (the leaky wave cavity, membrane and iris). This primary field is used to compute the distribution of the electric and magnetic fields across the spherical surface of the extended hemispherical lenses. The Fresnel transmission coefficients are used at the boundary to calculate the reflected and radiated field values. After the fields have been multiplied by the appropriate transmission coefficients, the equivalent and magnetic current densities are determined just outside the spherical surface. From these currents, the far fields are then calculated by integrating over the lens surface. For the cases considered in this chapter, the lens is not placed in the reactive near-field region of the feed, but in the radiative region, and therefore the PO can still be performed.

The aim is to design the lens for optimal performance in terms of a gain and optical coupling to a Gaussian beam (Gaussianity) for a certain aperture diameter  $D$ . Thus, the lens needs to have at a certain height,  $H$ , and it needs to be placed at a certain distance from the feed  $W$  (see the scheme of Figure 11.24a). The procedure to design the dielectric lens antenna for a certain diameter/aperture is the following:

- The waveguide, double slot and air cavity are designed at the central frequency, in the example is 550GHz. The double slot dimensions are optimized with a full wave simulator for maximum radiation efficiency. The electric field components in the cavity plane are exported from the 3D simulator into a custom-made program that will perform the optimization of the lens geometry.
- The optimum distance  $W$  is determined based on the frequency, the feed antenna illumination and the diameter of the lens. First, the taper edge angle  $\theta_f$  associated with the field level at the edge of the lens aperture is determined for a certain  $\rho$ . For example, a taper of 12dB,  $Te[12dB]$ , means that the field level at the edge of the lens diameter is 12dB below the field level at the broadside direction of the lens. The field taper is chosen according to the tradeoff between the spillover loss and the taper efficiency. The taper efficiency expresses the uniformity of the field distribution on the aperture of the lens. The optimum taper is between 10dB and 14dB, similar to reflector antennas.

Thus, we will compute the field from the antenna feed inside the silicon for certain distances (in the near or far-field depending on the distance) and compute the taper edge angle  $\theta_f$  for a taper field of  $Te[10dB]$ ,  $Te[12dB]$  and  $Te[14dB]$ . The intersection of these values with the theoretical value of the taper for a fixed aperture  $\theta_f = \sin^{-1}(D/2\rho)$  will give the optimum distance where the lens should be placed. An example is shown in Figure 11.23b, where the dashed lines present the taper angle obtained from the computation and the solid lines present the theoretical value of the taper for a diameter of 2.4mm. Thus, for a lens aperture of  $D = 2.4\text{mm}$  and a taper of  $Te[12dB]$ , the lens aperture should be placed at  $W = \sqrt{\rho_{opt}^2 - (D/2)^2} = 3.8\text{mm}$ . This computation is essential when the lens is placed in the near field of the primary feed, as it can be noted in Figure 11.23b, when we look at the dependency between the distance and the taper angle. When we move towards the far-field region this dependency fades, and the curves in Figure 11.23b get flatten ( $\theta_f$  becomes a constant with  $\rho$ ).

- Once the optimum distance  $W$  is set for a certain diameter, the optimum height of the lens  $H$  can be tuned to achieve maximum of directivity or taper efficiency. This tuning performs the optimization of the phase error associated to the phase center displacement and the phase error associated to the fact that the extended hemispherical lens is not quite an ellipse. In general, the larger the diameter, the higher the optimum height. Following the previous example, for a lens of 2.4mm at 550GHz the optimum lens height is  $H = 181\mu\text{m}$  which provides a directivity of 22.2dB (see Figure 11.24b). The gain includes spillover losses and the reflection losses inside the lens with and without the use of a matching layer. The reflections due to the use of high dielectric substrates can strongly impact the performance of the antenna, causing a large power loss. As Figure 11.24b shows, the total gain improves by 2dB because of the use of a matching layer. The optimum matching layer is designed with a dielectric of  $\varepsilon_m = \sqrt{\varepsilon_{si}}$  and has a thickness of  $\lambda_m/4 = \lambda_0/4\sqrt{\varepsilon_m}$ , being  $\lambda_0$  the wavelength at the desired central frequency. Since this antenna has a relatively narrow band, the use of one matching layer will be sufficient to

cover the whole band. The frequency behavior of the resulting antenna is shown in Figure 11.24c, where the directivity, the gain with and without matching layer and the Gaussicity are presented as a function of the frequency.

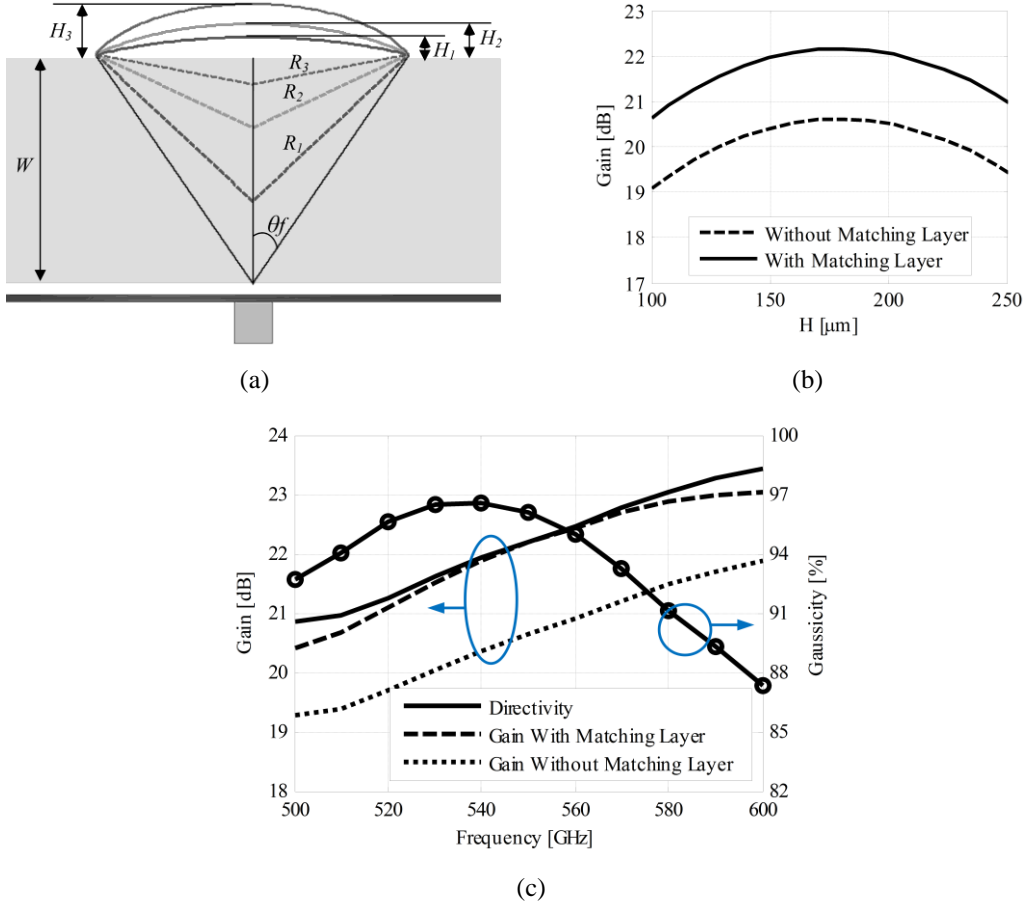


**Figure 11.24.** (a) Sketch of the dependency between the lens height  $H$  and the radius of the extended hemispherical lens. (b) Gain with and without matching layer as a function of the lens height  $H$ . (b) Directivity and gain as a function of the frequency with and without matching layer (left axis), Gaussicity as a function of the frequency (right axis).

### 11.3.3. Fabrication and Assembly

As it has been previously mentioned in the introduction, advanced fabrication processes and techniques are often required when working at terahertz frequencies, and it is one of the major constraints when designing these antennas. Silicon dielectric lens antennas have the advantage that the whole antenna can be fabricated using a silicon micromachining process, which provides excellent precision and accuracy, as well as a high level of integration with front-end transceivers.

For instance, the silicon lens fed by the leaky wave waveguide feed can be completely discretized among silicon wafers, processed with a DRIE silicon micromachining process and then stacked together. Specifically, it can be assembled in three parts: the first one is the leaky waveguide feed that contains waveguide, membrane and air-cavity; the second one are the blank silicon wafers required to achieve the correct thickness of the lens,  $W$ , and the third one is the lens surface. The following sections describe in detail the fabrication process for the two main parts.

### 11.3.4. Fabrication of the Leaky Wave Waveguide Feed

The three elements of the feed are the waveguide, the membrane with a double slot and the  $\lambda_0/2$  air cavity. All three can be fabricated on the same double SOI wafer, using a three-step etch process.

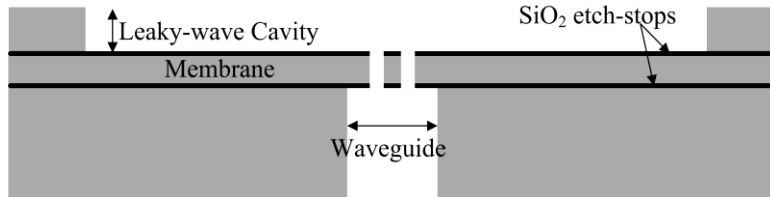


**Figure 11.25.** Sketch of the etching steps in the SOI wafer for the leaky wave waveguide feed fabrication.

The double SOI wafer sketch is presented in Figure 11.25, and it contains two  $\text{SiO}_2$  layers that act as etch stops to define the boundaries of the air cavity, the membrane with the iris and the waveguide length. For the leaky wave feed example shown in Figure 11.21, designed at 550GHz, the SOI wafer scheme consists of: 272 $\mu\text{m}$  of silicon that provides the depth for the air cavity, a 250nm layer of  $\text{SiO}_2$  as the etch-stop, a silicon layer 17 $\mu\text{m}$  thick as the membrane for the iris, another 250nm layer of  $\text{SiO}_2$  as the etch stop and a final silicon layer of 995 $\mu\text{m}$  for the rectangular waveguide.

The wafer can be patterned using conventional photolithographic techniques over the photoresist. The etching of the silicon can be performed using DRIE processes for deep selective silicon trenches which can achieve a selectivity of 300:1. The  $\text{SiO}_2$  features can be etched using inducted coupled plasmas (ICP). Both DRIE and ICP allow the fabrication of clean and perfectly controlled silicon membranes.

After etching, both sides of the SOI wafer are sputtered with gold to metallize the waveguide and iris. A uniform coverage can be achieved by a good optimization of the sputtering process, even in structures that contain vertical walls with high aspect ratios.

### 11.3.5. Fabrication of the Shallow Silicon Lens

The fabrication of the shallow silicon lens consists of a single photolithographic process that can control the diameter, height and curvature of the lens, based on control of the shape of the deposited photoresist and the etching selectivity between the photoresist and the silicon.

The basic idea is to transfer the lens shape into a photoresist lens and transfer the shape onto the silicon wafer by a DRIE process as Figure 11.26 shows. The process consists of four steps:

- 1) Deposit a thick layer of photoresist and pattern it with the desired lens aperture using conventional photolithographic process.
- 2) Reflow the photoresist pattern with heat in order to obtain the lens profile. By coating the photoresist above the glass transition temperature, the surface tension applied to the photoresist makes the photoresist to reflow in the resulting spherical shape of the lens.
- 3) Etch the photoresist and silicon simultaneously with a DRIE process.
- 4) The process finishes when a complete etching is achieved and the lens profile is transferred to the silicon wafer.

This process can control both the diameter and the curvature of silicon lens. The diameter of the lens depends on the thickness of the photoresist that can be coated and patterned. So far, the lens diameter of around 6.5mm with a height of 400 $\mu\text{m}$  has been successfully micro-fabricated as in [63]. Here, we will focus on a lens fabricated with a diameter of 3mm that will follow the example at 550GHz. The curvature of the shallow lens can be controlled by two process variables:

- Amount of photoresist: The pattern and the height of the photoresist applied onto the silicon wafer will determine the curvature of the resulting lens. The thicker the photoresist deposited, the thicker the lens can be.
- Etching selectivity applied to the photoresist and silicon: The curvature of the silicon lens can be controlled by the adjusting the selectivity between of the silicon and photoresist, which is optimized by controlling the gas ratio between the  $\text{CF}_4$  and  $\text{O}_2$ , the bias power and RF power.

For example, if the etching selectivity is 1:3, meaning 1 unit of photoresist etches three times the rate of the silicon, the curvature of the silicon lens will be three times higher than the curvature of the photoresist lens. In the lens shown in Figure 11.27, the original height of photoresist was 210 $\mu\text{m}$  but because the etching selectivity was 1:3, the height of the silicon lens was around 280 $\mu\text{m}$ .

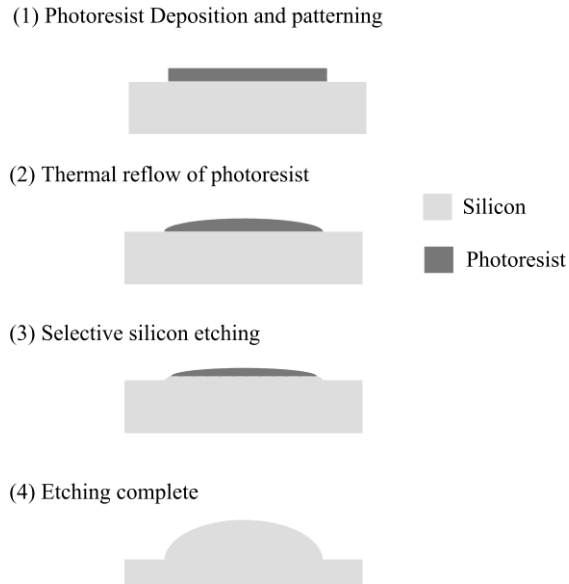


**Figure 11.26.** Sketch of the silicon lens fabrication process using photolithographic techniques.

The surface roughness achieved with this process on the silicon lens is better than 0.5 $\mu\text{m}$  which is more than sufficient for terahertz frequencies.

The use of a matching layer on dielectric lenses is essential to reduce the high reflection losses produced by the use of high permittivity substrates. At terahertz frequencies the material that is commonly used as a matching layer for silicon lenses is Parylene. It has a permittivity of 2.69 which is not ideal for silicon (the optimum permittivity for a matching layer for a silicon lens would be  $\epsilon_m = \sqrt{11.9} = 3.45$ ) but close enough to reduce considerably the losses by reflection. Also, Parylene polymer coatings can be applied using vapor deposition equipment, which allows a very conformal deposition with high control of the coating rate and thickness. The dimer (Parylene-C) is vaporized under vacuum and heat to form a dimeric gas. The gas is pyrolyzed to transform it into its monomeric form so it can be deposited as a transparent polymer film.

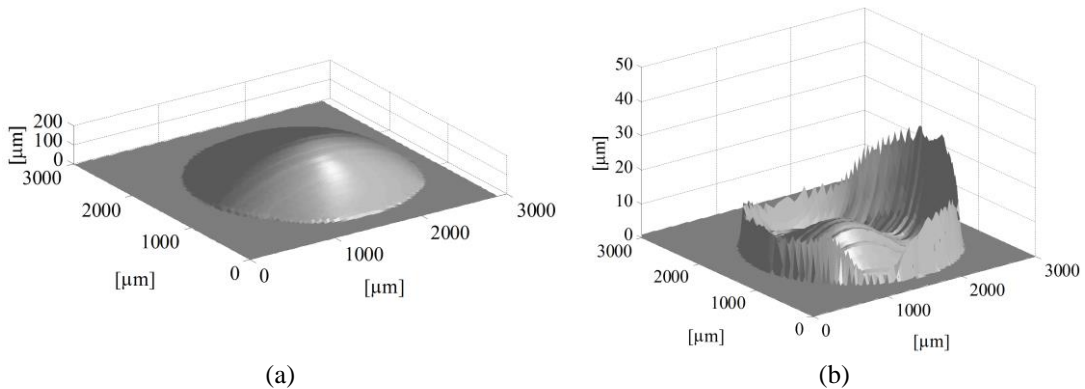


**Figure 11.27.** (a) Resulting scanning of the fabricated lens profile. (b) Error Surface between the fabricated lens profile and a spherical surface.

Characterizing the accuracy of the fabricated lens compared to an ideal hemispherical lens has been the key for understanding and optimizing the fabrication. The surface of the fabricated lens can be characterized and studied from the mapping performed by a surface profilometer. In order to study how the fabricated surface resembles a sphere, we can use the optimization toolbox in Matlab to compute the sphere dimensions. The sphere has a certain radius,  $R$ , aperture diameter,  $D$ , sphere height,  $H$ , that minimizes the error with the fabricated surface. For the example of the fabricated lens shown in Figure 11.27a, the optimum dimensions were  $R = 3.90\text{mm}$ ,  $D = 2.93\text{mm}$  and  $H = 285.6\mu\text{m}$ , and the standard deviation of the error was  $\sigma = 18.36\mu\text{m} = 0.11\lambda_{\text{Si}}$ . From the error surface (see Figure 11.27b) we can see that the highest error is contained in the edges of the lens. For instance, if  $100\mu\text{m}$  of the edges of the lens are not considered, the standard deviation goes down to  $\sigma = 5.4\mu\text{m} = 0.04\lambda_{\text{Si}}$ . This adjustment in the illumination can be achieved by the tuning of the wafer thickness,  $W$ , which in this case will be designed to obtain a field taper of  $-14\text{dB}$  at the border of this new effective lens aperture. Thus, by reducing the wafer thickness from the original  $W = 3.8\text{mm}$  to  $W = 3.21\text{mm}$ , we will reduce the effective diameter of the lens from  $2.93\text{mm}$  to  $2.38\text{mm}$ .

The effect of this aberrations can be understood as a phase distortion in the aperture field of the lens. Assuming a tapered Gaussian aperture of the diameter of the lens we can estimate what would be the effect of this phase error over the radiation pattern. For the error surface shown in Figure 11.27b, the lens distortion would correspond to an increase of the secondary lobes in the radiation pattern and a tilt in the main direction of the main beam, as Figure 11.28 shows.

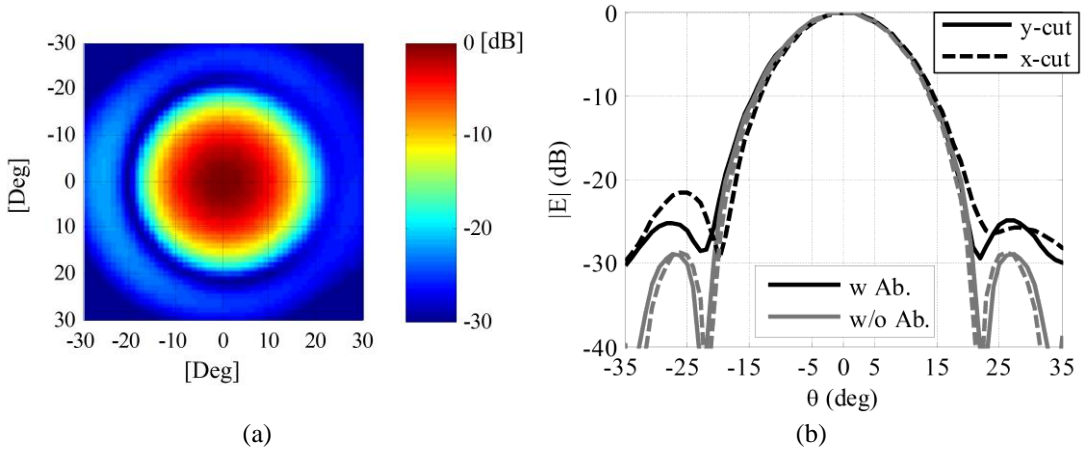


**Figure 11.28.** (a) 2D and (b) 1D cuts of the radiation pattern of a Gaussian aperture with a field taper of  $14\text{dB}$  which contains the aberrations of the fabricated micro-lens at  $550\text{GHz}$ .

### 11.3.6. Silicon Micro-Lens antenna performance and limitations

The key advantage of using this silicon dielectric lens antenna at terahertz frequencies is the fact that the lens antenna can be fabricated entirely using a silicon micromachining process. This means that from the simple processing of one wafer, over thousands of elements can be obtained. Figure 11.29, shows some examples of silicon lens arrays fabricated with this technology, with diameters of  $1\text{mm}$ ,  $3\text{mm}$ , and  $6.5\text{mm}$ .

Lenses from the arrays (shown in Figure 11.29) were scanned to check their accuracy [62]. The agreement to a spherical profile is good particularly for the small lenses (see Figure 11.29). From the prototypes, several lens profiles have been studied with the technique presented before, and even individual antenna lens prototypes have been fabricated and measured. In this section we will present one of the published prototypes in [56] to give an idea of how the assembly and measurements were performed.

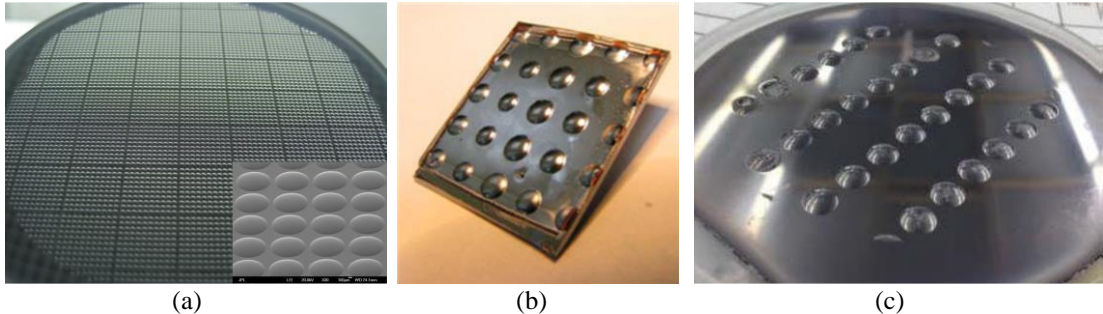


**Figure 11.29.** Examples of lens arrays manufactured using silicon micro-machining processes (a) One of the first  $5 \times 5$  lens array of  $D = 2.5\text{mm}$ , (b) 50 arrays of  $10 \times 10$  lenses of  $D = 1.5\text{mm}$ , (c) 4 linear arrays of 6 and 8 lenses of  $D = 6.4\text{mm}$ .

Figure 11.32 shows the lens and the iris prototype at 550GHz. Both pieces are assembled using metal pins that provides alignment and screws that provide the pressure to the wafers. The thickness between the lens and leaky wave is optimized for the illumination of an effective diameter of 2.39 and reduce the aberrations from the fabricated profile. To achieve the desired thickness, five silicon wafers are placed in between. These silicon wafers, as well as the lens wafers, need to be of high resistivity, i.e. of  $10\text{k}\Omega\cdot\text{cm}$ , in order to lower the dielectric loss. In this prototype  $10\text{k}\Omega\cdot\text{cm}$ , the dielectric losses are calculated to be around 0.06dB for the entire silicon stack. Moreover, double sided polished wafers are employed in order to have good surface contact between all the wafers, avoiding air gaps.

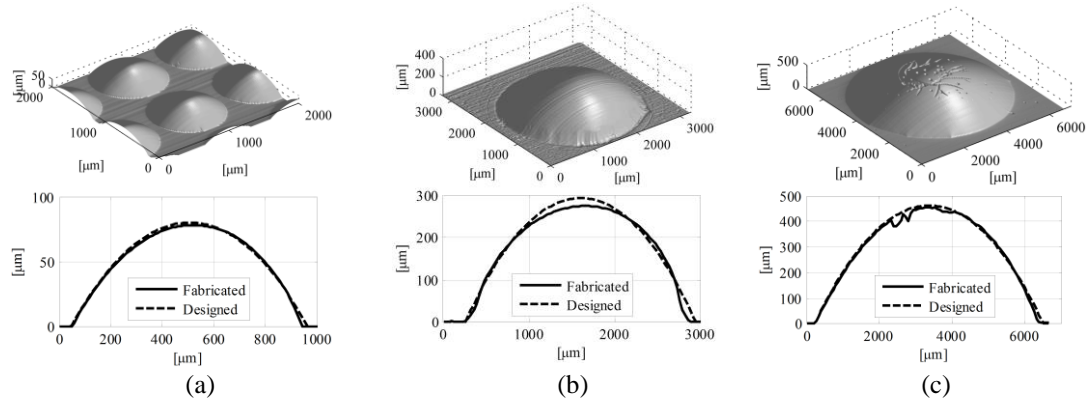


**Figure 11.30.** Examples of fabricated lenses with diameters (a)  $1.5\text{mm}$ , (b)  $2.5\text{mm}$  and (c)  $6.5\text{mm}$ , and their comparison with a perfect hemispherical surface.

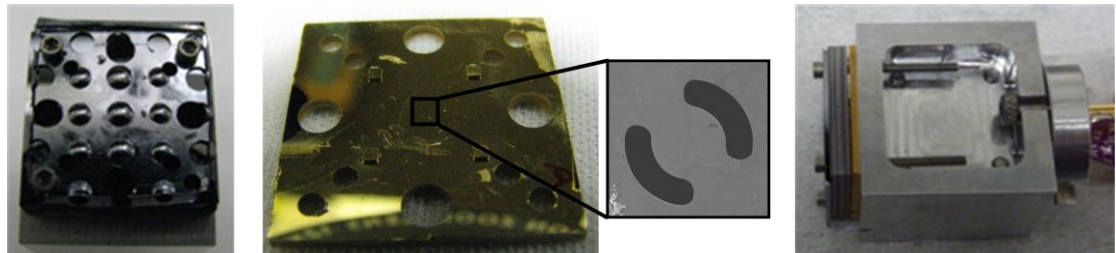


**Figure 11.31.** Photograph of the fabricated prototype at 550GHz.

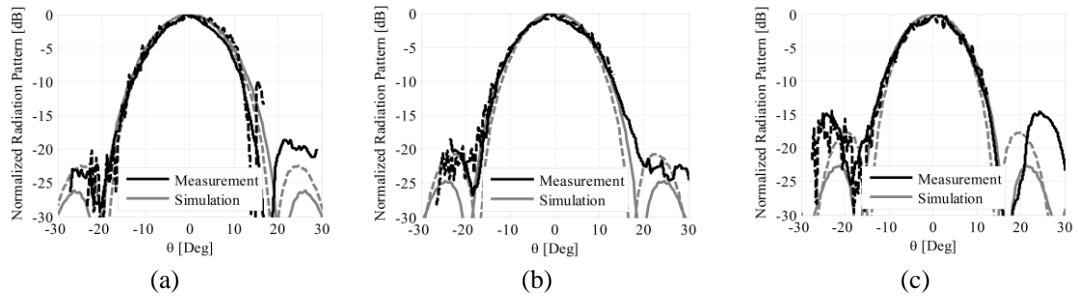


**Figure 11.32.** Measurements of the radiation patterns at 530GHz, 550GHz and 590 GHz. The solid lines correspond to the E-Plane and dashed line to the H-Plane.

Radiation pattern measurements were performed of the prototype at 550GHz. Figure 11.32 presents the E and H planes (solid and dashed lines respectively) of the measured normalized radiation pattern at 530GHz, 550GHz and 590GHz. The agreement with the simulations (shown in grey) is very good. Well focused beams were achieved, and the difference with the simulations were primarily due to a small misalignment between the lens and the antenna feed and, as it was portrayed before, the aberrations of the shallow lens surface that would increase the secondary lobes and a tilt on the radiation pattern.

The results achieved so far show a great potential to use these dielectric lens antennas in the development of future focal plane arrays at terahertz frequencies. By using the leaky wave waveguide feed, we only need a small part of the surface of the lens, which reduces the reflection losses and phase errors that these type of lenses suffer. But most of all, it allows the use of photolithographic process when fabricating the lens. The fabrication of the lenses using photolithographic process reduces the cost, with the same performance achieved with other fabrication methods, such as laser micromachining. At the moment, it is still difficult to predict precisely some of the lens parameters in the fabrication, particularly the curvature, when we millimeter diameter silicon lenses are attempted. However, by characterizing accurately the fabricated profiles, we can compensate the aberrations and still obtain very good performances while continuing to keep improve the fabrication process of these lenses.

## 11.4. Terahertz modulated metasurface antennas

The reader can find a comprehensive description of the analysis and design of modulated metasurface (MTS) antennas in Chapter 13. These antennas analyzed consist of planar apertures made of sub-wavelength patches printed on a grounded dielectric slab. This class of antenna is, thus, inherently flat and presents a low mass. Its most attractive feature is the capability of obtaining high- to very-high gains with low-profile structures. Indeed, the aforementioned characteristics make modulated MTSs particularly appealing for space [64]-[65]. Among their other advantages it is important to note their capability of conforming to curved surfaces [66], and providing a simple on-surface control of the aperture fields for beam shaping, pointing and scanning.

### 11.4.1 Sinusoidally Modulated Inductive Surfaces

Radiation by modulated MTS stems from the interaction of a surface-wave (SW), which can be launched using a coaxial pin, and a modulated inductive plane, realized in the microwave range by means of printed sub-wavelength patches [64]-[65]. The interaction between the SW and the periodic modulation makes the (-1) indexed Floquet mode enter the visible region so it becomes a radiating mode. To illustrate the concept, let us consider a scalar one-dimensional modulation at the  $z=0$  plane, invariant in the  $y$  direction, and with propagation along  $x$ . The sinusoidally modulated inductance can be written as

$$X_s(x) = \bar{X} \left( 1 + M \sin\left(\frac{2\pi}{d}x\right) \right) \quad (11.10)$$

where  $\bar{X}$  is the average surface reactance,  $M$  is the modulation factor and  $d$  is the period of the modulation. This case was studied by Oliner and Hessel in [67]. The solution to the periodic problem consists in an infinite series of Floquet modes, the transverse-to- $z$  wavenumber for the  $n$ -indexed mode is

$$k_{t,n} = \beta_{sw} + \beta_\Delta - j\alpha + 2\pi n / d \quad (11.11)$$

where  $\beta_\Delta$  and  $\alpha$  are perturbations in the phase and attenuation constants, respectively, which depend on  $\bar{X}$ ,  $M$  and  $d$ . In turn,  $\beta_{sw}$  stands for the unperturbed value of  $k_t$  ( $M = 0$ ), obtained by imposing the transverse resonance condition between  $j\bar{X}$  and the free-space TM impedance

$$j\bar{X} + Z_{0,TM} = 0 \quad (11.12)$$

Given that we are looking for SWs  $\beta_{sw} > k$  and  $Z_{0,TM} = -j\zeta\sqrt{\beta_{sw}^2 - k^2} / k$ , with  $k$  and  $\zeta$  being the free-space wavenumber and impedance, respectively. Solving for  $\beta_{sw}$  in (11.12) gives  $\beta_{sw} = k\sqrt{1 + (\bar{X}/\zeta)^2}$ . When  $|\Re\{k_{t,n}\}| < k$ , the corresponding mode enters in the visible region of the spectrum, and it can be identified as a leaky wave solution. The  $n = -1$  mode is the dominant leaky-mode, and it radiates in a direction given by

$$\beta_{sw} + \beta_\Delta - 2\pi / d = k \sin \theta_0 \quad (11.13)$$

where  $\theta_0$  is the angle with respect to the  $z$  axis. Consequently, for a single beam directed at an angle  $\theta_0$ ,  $\bar{X}$  and  $d$  can be related using  $\beta_{sw} = k\sqrt{1 + (\bar{X}/\zeta)^2}$  in (11.13). For instance, given a free-space wavelength  $\lambda$ , one can generate a single forward beam using a period

$$d = \lambda / \left( \sqrt{1 + (\bar{X}/\zeta)^2} - \sin \theta_0 \right) \quad (11.14)$$

when  $\bar{X}/\zeta > \sqrt{4 \sin \theta_0 (1 + \sin \theta_0)}$ . In the derivation of (11.14), the effect of  $\beta_\Delta$  ( $\ll \beta_{sw}$ ) has been neglected.

### 11.4.2 Constituent Elements for THz metasurfaces

As mentioned in Section 11.4.1, one can implement modulated MTSs by artificial surfaces realized with sub-wavelength patches, which offer a good performance below 100 GHz. However, there are some aspects which hinder their use in terahertz (THz) antennas. First, the losses in the dielectric become, in most applications, a limiting factor, so all-metal structures are preferred. Second, it is challenging to combine a coaxial SW launcher with the rectangular waveguide (RW) output of solid-state frequency-multiplied continuous-wave sources, which are the most commonly used sources at THz frequencies [68]. One could, alternatively, use a graphene sheet transferred onto a back-metallized substrate to realize the modulated impedance plane [69]. Such modulation is achieved via graphene's field effect by applying adequate DC bias voltages to gating pads beneath the graphene sheet. However, the bias network renders the structure more complex, and graphene cannot be used to realize anisotropic inductance surfaces, which limits the degree of control on the aperture fields.

In the remainder of this section, we will show the suitability of silicon micromachined elements for modulated MTS antennas in the THz range. Among the existing techniques, deep reactive ion etching (DRIE) is particularly well-adapted for micromachining sub-wavelength features at sub-millimeter wavelengths. Since it is based on etching, one may argue that it is challenging to maintain straight sidewalls and uniform depth across the wafer for each depth step. Nevertheless, these drawbacks can be overcome by extensive process development [31]-[70] and a thorough design. After carrying out the desired number of etching steps, 2  $\mu\text{m}$  of gold is deposited by sputtering to metallize the structure.

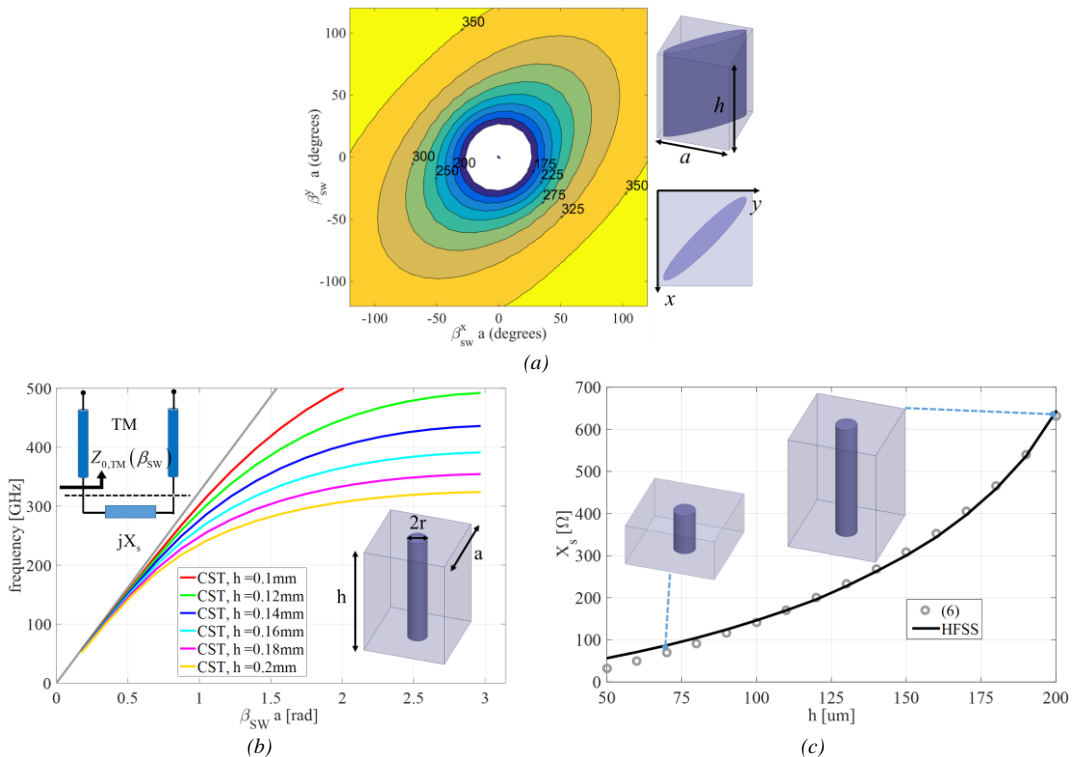


**Figure 11.33.** (a) Isofrequency dispersion contours for the unit cell depicted in the insets. The unit cell's side is  $a = 138.5 \mu\text{m}$ , the height of the cylinder is  $h = 180 \mu\text{m}$ , and the elliptical cross-section has minor axis equal to  $30 \mu\text{m}$  and axial ratio equal to 4. (b) Dispersion curves of the fundamental TM-SW modes propagating on a set of bed of nails. Each curve corresponds to an infinite array of cylinders of height  $h$ , radius  $r = 17.5 \mu\text{m}$ , and arranged on a square lattice with side  $a = 147 \mu\text{m}$ . Results obtained using the eigenmode solver in [76]. (c) Equivalent surface reactance of an infinite array of cylinders on a ground plane and arranged on a square lattice at 300 GHz, as a function of the height  $h$  of the cylinders. The radius of the cylinders is  $r = 17.5 \mu\text{m}$ , and the side of the unit cell is

$a = 147 \mu\text{m}$ . The solid line represents the values calculated solving (11.12) for  $\bar{\mathbf{X}}$ , after using in (11.12) the  $\beta_{\text{sw}}$  obtained for each  $h$  with a full-wave eigenmode solver [76].

The proposed MTS consists in an array of metallic cylinders of elliptical cross-section (see insets in Figure 11.32, placed on a ground plane and arranged in a square lattice with sub-wavelength unit cell size [71]-[72]. Such a structure, which resembles a Fakir's bed of nails, has been used in the past for synthesizing artificial surfaces of inductive nature [73], and can be easily fabricated using DRIE. The surface reactance corresponding to an elliptical cylinder is, in general, a tensor, which depends on the transverse wave vector  $\underline{\beta}_{\text{sw}} = \beta_{\text{sw}}^x \hat{x} + \beta_{\text{sw}}^y \hat{y}$  and relates the transverse electric and magnetic fields (evaluated at the upper interface) as  $\vec{E}_t|_{z=0^+} = j\underline{\underline{X}}_S \cdot \hat{z} \times \mathbf{H}_t|_{z=0^+}$ , where  $\underline{\underline{X}}_S = [[X_{xx} X_{yx}]^T [X_{xy} X_{yy}]^T]$  is defined in Cartesian coordinates, and  $\hat{z}$  is the normal to the MTS plane.

The elliptical cylinder possesses two orthogonal symmetry axes, which principal directions can be identified, in the low frequency regime, with the principal axes of the dispersion ellipse. By dispersion ellipse we denote the curve that, for a fixed frequency, provides the  $\beta_{\text{sw}}^x - \beta_{\text{sw}}^y$  pairs corresponding to waves propagating at such a frequency. The surface reactance tensor at a given frequency can be retrieved from its isofrequency dispersion ellipse by fitting, in the least square sense, the simulated data with [74]

$$\begin{aligned} & (1 + X_{xx} X_{yy} - X_{xy} X_{yx}) k k_z + (X_{xy} + X_{yx}) \beta_{\text{sw}}^x \beta_{\text{sw}}^y \\ & + \left[ (X_{xx} + X_{yy}) k^2 - X_{xx} (\beta_{\text{sw}}^y)^2 - X_{yy} (\beta_{\text{sw}}^x)^2 \right] = 0 \end{aligned} \quad (11.15)$$

where  $k_z = \sqrt{(\beta_{\text{sw}}^x)^2 + (\beta_{\text{sw}}^y)^2 - k^2}$ . Figure 11.33a shows the isofrequency dispersion ellipses for an elliptical cylinder with minor axis equal to  $30 \mu\text{m}$  and axial ratio equal to 4, in a square unit cell with side  $a = 138.5 \mu\text{m}$ . This case presents at 300~GHz an artificial tensor surface with  $\underline{\underline{X}}_S = \zeta [[1.04, 0.46]^T [0.46, 1.03]^T]$ . By changing the height, orientation and axial ratio of the elliptical cylinders, each component of the tensor will undergo a different modulation. This feature is exploited to get the required degrees of freedom to control the aperture fields [65],[75].

In the limiting case of a circular cross-section, for electrically small period, the isofrequency dispersion ellipse becomes a circumference and the surface reactance is scalar. Figure 11.32b shows the dispersion curves (obtained with the eigenmode solver of a commercial software) [76] of the fundamental TM-SW modes propagating on a set of bed of nails. Each curve corresponds to an infinite array of cylinders with a given height  $h$ , radius  $r = 17.5 \mu\text{m}$ , and arranged on a square lattice with side  $a$ . The period  $d$  has been computed at 300 GHz using (11.14) for an average impedance  $\bar{X} = 0.7\zeta$  and a forward beam pointing at  $\theta_0 = 5^\circ$ , which for  $N = 6$  implies  $a = 147 \mu\text{m}$ . The surface reactances retrieved through (11.12) are shown in Figure 11.32c. Unfortunately, long cylindrical rods are difficult to realize with DRIE while keeping a good precision and a simple process. Therefore, upon choosing  $\bar{X}$  and  $N$ , one has to verify that the required heights satisfy  $h/r \leq 10$  before proceeding with the design. Modulated surface reactances can be realized using the data in Figure 11.32c under a local periodicity assumption.

### 11.4.2 Design example

The design below consists in a spirally modulated MTS antenna. The spiral has been designed at 300 GHz and it provides a broadside pencil beam with circular polarization. The synthesized surface reactance is

$$X_s(x) = \bar{X} \left( 1 + M \sin \left( \frac{2\pi}{d} \rho - \phi \right) \right) \quad (11.16)$$

where  $\rho$  and  $\phi$  represent the position on the MTS plane in polar coordinates. The reader is referred to [65] for further details. In our case,  $\bar{X} = 0.7\zeta$ ,  $M = 0.65$ ,  $N = 6$  and  $a = 138.5 \mu\text{m}$ . The structure is shown in Figure 11.33a, where each color represents a different height of the metallic cylinders. Figure 11.33b

shows a SEM picture of a portion of the bed of nails fabricated using DRIE. The structure is fed with an overmoded circular waveguide with only the  $\text{TM}_{01}$  mode propagating, this mode provides an efficient excitation of the TM surface wave on the MTS plane, while avoiding the use of a coaxial feed. The feeder (not shown here) is placed underneath the MTS and it transforms the  $\text{TE}_{10}$  mode in the input RW to the  $\text{TM}_{01}$  in the CW. The magnitude of the  $S_{11}$  in dB obtained with the aforementioned feeding structure is shown in Figure 11.33c. The far-field gain patterns have been computed with HFSS [76] and they are shown in Figure 11.33d for two orthogonal planes at 300 GHz. A similar performance has been verified for the patterns in the rest of the 290-315 GHz band.

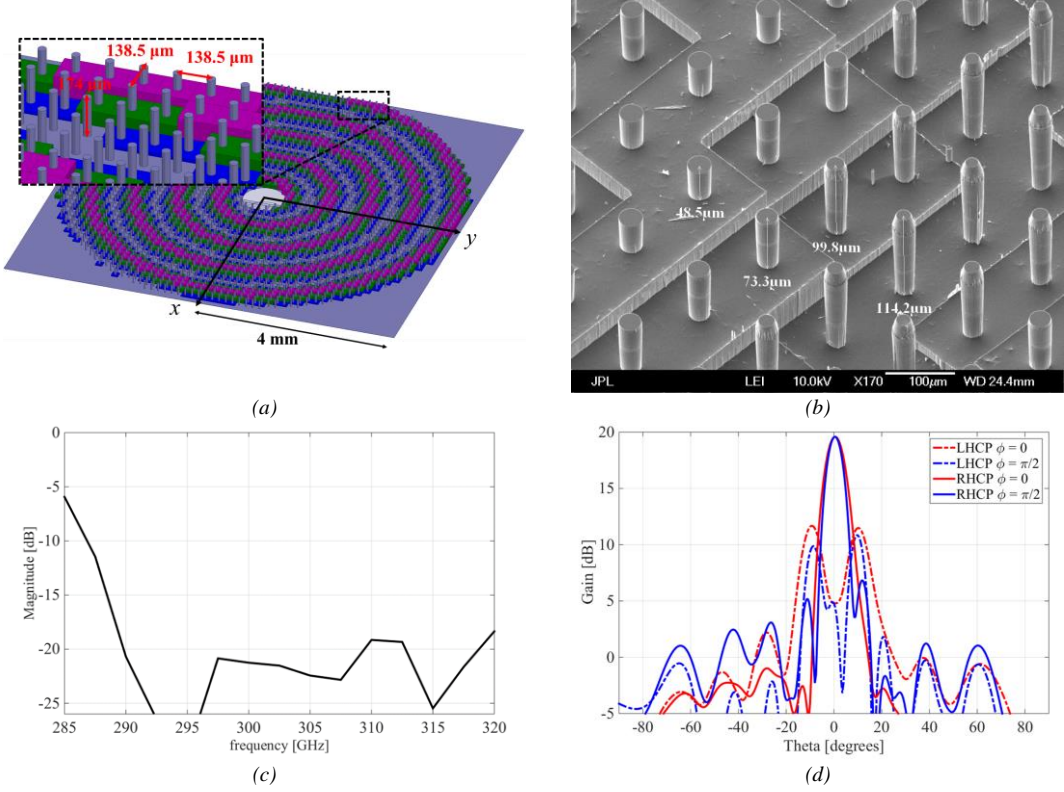


**Figure 11.34.** (a) Simulated spiral modulated MTS antenna. (b) SEM picture of a bed of nails fabricated by means of DRIE. (c) Magnitude of the  $S_{11}$  in dB at the input RW port of the antenna. (d) Right-handed circular polarized (RHCP) and left-handed circular polarized (LHCP) gain patterns at 300 GHz plotted with solid and dashed lines, respectively, on two orthogonal cuts.

## 11.5. CMOS antennas

Complementary metal oxide semiconductor (CMOS) technology has recently made tremendous improvement in millimeter-wave capabilities because of the aggressive technology scaling during the past decade. As a demonstration of this rapid progress, full transceivers have been demonstrated in the millimeter-wave band [77],[78]. More recently, the NASA's Jet Propulsion Laboratory has extensively studied the applicability of system-on-chip communication, radar, and spectrometer terahertz solutions to the exploration of planets and moons in the outer solar system.

CMOS technology offers a pathway to improve the payload size, weight, and power of instruments and telecom systems on spacecraft directly through higher levels of integration and added calibration functionality. In Figure 11.35, a mm-wave receiver of an existing radiometer / spectrometer pixel is compared to a receiver fully implemented in System on Chip (SoC) technology.

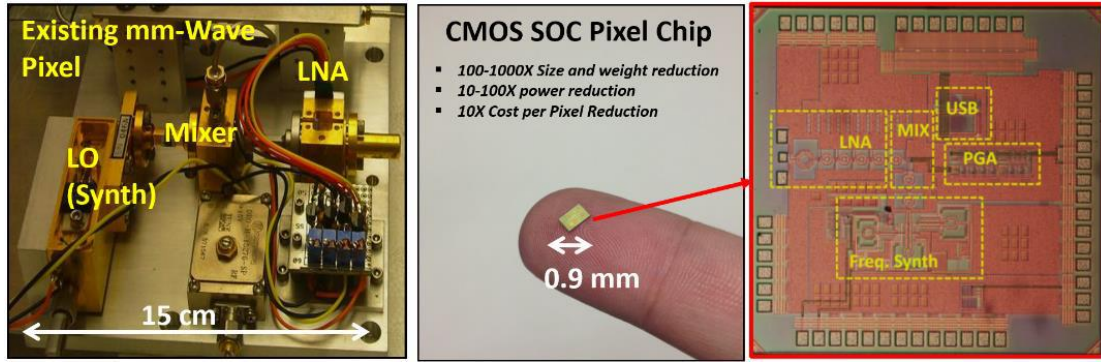


**Figure 11.35.** Comparison of size between existing mm-wave receiver of an existing radiometer/spectrometer pixel and a receiver implemented in System on Chip (SoC) technology.

In the past few years, NASA's Jet Propulsion Laboratory in collaboration with UCLA, has been exploring the use of CMOS SoC in millimeter-wave and terahertz instruments [79]-[83]. The severe metal density rules imposed to the CMOS fabrication process, making efficient on-chip antennas almost impossible to implement, can be overcome by using off-chip antennas with beam-lead interconnections [79]. The beam-lead interconnection appears to be an excellent interconnection technique for CMOS circuits at terahertz frequencies that can be applied to ground signal (GS) pads (i.e. differential line) and GSG pads (CPW line) as shown in Figure 11.36.

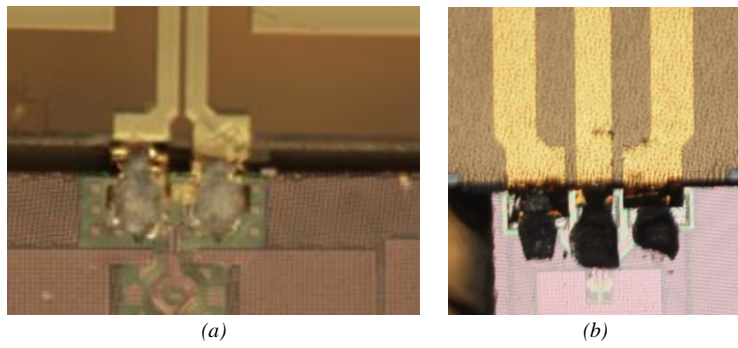


**Figure 11.36.** Example of beam-lead interconnection for (a) ground-signal (GS) RFIC and (b) ground-signal-ground (GSG) pad RFIC.

Several beam-lead antennas designed as part of CMOS SoCs are discussed here. The antenna shown in Figure 11.37 consists of a micromachined silicon dipole antenna interconnected using the beam-lead technique. A dipole was selected as it naturally couples to the differential output of the CMOS device. The dipole is printed on a  $1\mu\text{m}$ -thick Silicon Nitride membrane ( $\text{Si}_3\text{N}_4$  with  $\epsilon_r=7.5$ ) [79]. The hatched area in Figure 11.37 is where the  $300\mu\text{m}$ -thick silicon wafer material is present below the  $\text{Si}_3\text{N}_4$ , while the light gray area surrounding the dipole is only made of the thin  $\text{Si}_3\text{N}_4$  membrane. The cavity thickness was chosen to align the antenna and the chip at the same height. As the distance between the radiating element and the PCB ground plane is about  $300\mu\text{m}$ , it increases the antenna directivity. In addition, two metal bars are employed in order to reduce backward radiations toward the chip that is made of lossy dielectric.

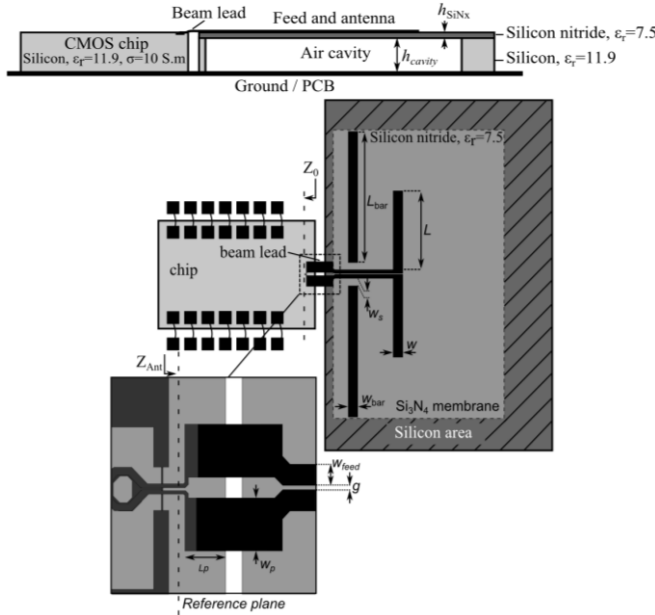


**Figure 11.37.** Dipole antenna integrated with the Tx CMOS chip [79]. (Top: cross section. Bottom: top view.

The antenna input impedance was matched to  $Z_{\text{Ant}}=Z_0^*=29 + j38 \Omega$ , where  $Z_0$  is the impedance of the chip. The fabricated antenna and its CMOS chip are shown in Figure 11.38. The antenna was measured at 154GHz (i.e. center frequency of the CMOS chip). This is an active measurement as the antenna is measured with its Tx CMOS chip. A standard pyramidal horn antenna was connected on one head of an ABmm measurement system and the CMOS chip prototype is connected to a DSP lock-in amplifier (Model SR830 from SRS, Sunnyvale, CA). Two rotating stages were employed to move the antenna in elevation and azimuth planes to scan the far-field. The measured and calculated radiation patterns are in good agreement as shown in Figure 11.39. Measurement have shown that the antenna can reach up to 70% efficiency near the lossy CMOS transmitter chip. The overall transmitter operating at 154GHz shows excellent performance as its effective isotropic radiated power (EIRP) and total radiated power (TRP) reach 20.6 dBm and 11.2 dBm, respectively [79].

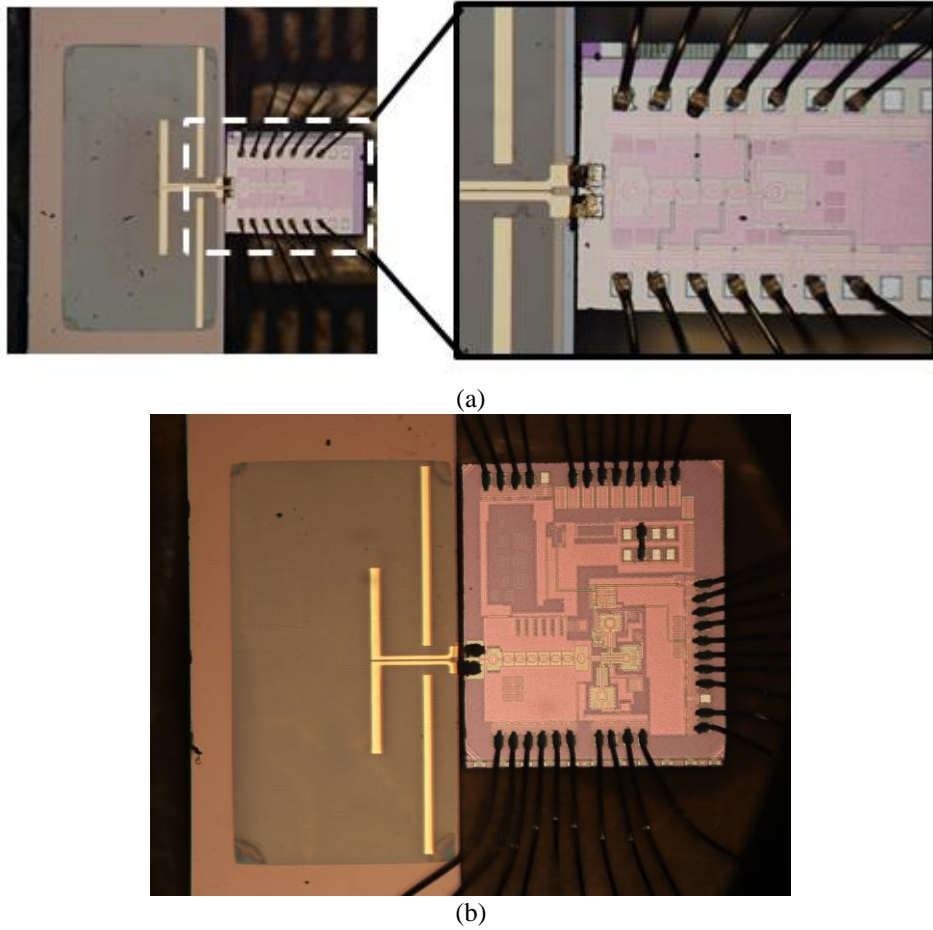


**Figure 11.38.** (a) Die photo of a proposed SoC Transmitter operating at 150GHz [79]. (b) Die photo of a 140 GHz transmit array for highly scalable multi-chip phase arrays [80].

This antenna was also used as part of a 65nm CMOS 140 GHz 27.3dBm EIRP transmit array. This transmit phased array offers beam steering capability [80]. It uses local phase-locked loop (PLL) reference generation system. Unlike traditional CMOS phased arrays, this enables the array to be formed over multiple chips while avoiding the challenges of distributing mm-wave signals between them. A  $2 \times 4$  multi-chip array prototype was fabricated and tested using the beam-lead dipole membrane antenna.

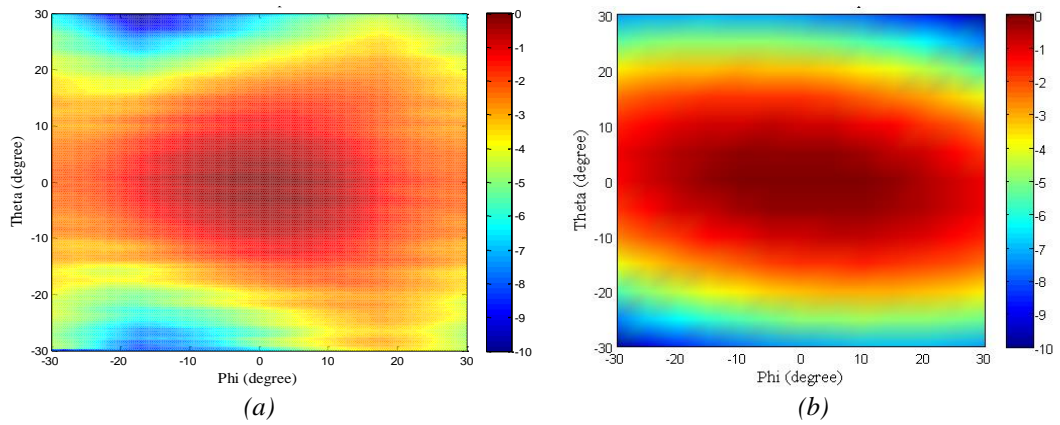


**Figure 11.39.** (a) Measured and (b) simulated normalized 2D radiation patterns of the CMOS off-chip dipole antenna at 154 GHz (co-polarization).

The antenna shown in Figure 11.40 was built on a high-resistivity Silicon substrate for a full CMOS

SoC navigation processor operating at 94GHz. This navigation processor can be used to safely guide unmanned aerial vehicles (UAVs) and unmanned ground vehicles (UGVs) through cluttered and urban environments while consuming very little payload [83]. The navigation system defines multiple pathways using mm-wave base-stations called path generators and then uses a single CMOS SoC containing a receiver, ADC and an FFT processor to detect and navigate these pathways. The demonstrated confined pathway SoC (CP-SoC) occupies 5.4mm<sup>2</sup> of silicon area in 65nm technology, and consumes only 199 mW, making it suitable for lightweight payloads associated with UAVs and UGVs.

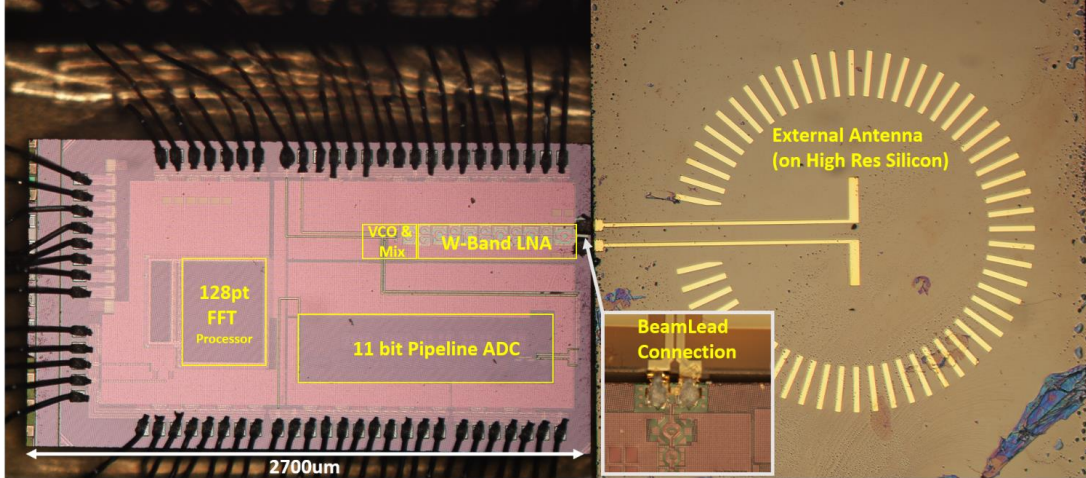


**Figure 11.40.** Die photo of the proposed SoC navigation processor combined with the external antenna module (on a HiRes Si substrate) used to capture incoming radiation [83].

## 11.6. Slot antennas in BICEP2

The measurement of the polarization of the cosmic microwave background (CMB) is the holy grail of present day cosmology. CMB contains the most valuable relic of the early universe [84]. The details of the structure and evolution of the universe are believed to be encoded in the anisotropy of the CMB. It is believed that the direct evidence of the inflationary epoch – the rapid expansion of the universe after the Big Bang – lies in the traces of gravitational waves in the CMB, which manifests in the temperature anisotropy and polarization of the CMB. If inflationary gravitational waves do indeed exist, they will be the oldest relic of the universe, created 500,000 years before the CMB was emitted. The measurement of the CMB polarization – the B-mode polarization in particular – will be the indirect proof of the existence of the inflationary gravitational waves and will give insight into the epoch of inflation.

CMB polarization detection instruments require large focal planes with thousands of detectors to have large throughput improving overall sensitivity of the instrument. To reduce stray radiation pickup, the field of view of these detectors needs to be restricted. The purpose of BICEP (i.e. Background Imaging of Cosmic Extragalactic Polarization) is to measure the polarization of the CMB radiation; in particular, to measure the B-mode of the CMB. In BICEP1, the first generation of the BICEP instruments, the collimation of the incoming beam is achieved using metal feed horns (Figure 11.41a). Even though feed horns have excellent performance, their mass, size, and expense make them unsuitable for large arrays with hundreds and thousands of pixels.

A monolithic array of antenna-coupled detectors on a planar substrate, which can be fabricated with photolithographic techniques, would solve the aforementioned problem. However, most planar antenna designs use thin dielectric substrate to avoid excitation of surface waves, and they produce broad beam patterns. Most often, they require substrate lenses or micro-machined horns for efficient coupling to the telescope optics. As a significant improvement, the second generation instrument BICEP2 uses a novel dual-polarization planar slot antenna phased array which produces quite a narrow beam with no additional optical coupling elements. The output from the antenna array is two superconducting thin-film microstrip lines, one for each polarization, which can be efficiently coupled to bolometer detectors [6] to produce a single pixel in an imaging focal plane array. Figure 11.41 illustrates the BICEP1 and BICEP2 instruments.

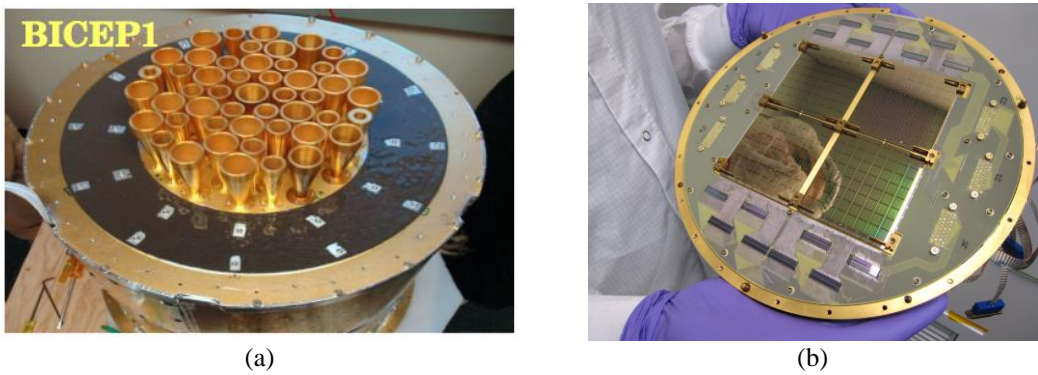


**Figure 11.41.** (a) BICEP1 antenna using feed horns with different apertures. (b) BICEP2 antenna using planar dual-polarized phased arrays

The “T” shaped dual-polarized antenna structure chosen for this work is ideal for low cross-polarization performance. The T-slots were arrayed in a compact architecture to form the slot array antenna.

The antenna is fabricated on a high dielectric silicon substrate ( $\epsilon_r = 11.8$ ) with thickness between  $\frac{3}{4} \lambda_g$  and  $\lambda_g$ . The slots are illuminated through substrate to take advantage of the stronger antenna response on the dielectric side. A quarter wavelength thick quartz, whose dielectric constant is optimum for silicon anti-reflection coating, is used on the silicon substrate to minimize reflection at the air-substrate interface.

Due to the thick dielectric substrate, excitation of the lossy grating lobes for the array is a concern. The antenna slots in each detector must be spaced to Nyquist sample the focal plane surface to avoid generating the grating lobes. The radiation pattern of each axis of an array is calculated from the N

elements per linear dimension spaced at distance  $S$  as follows:

$$A(\theta) = \sum_{m=-(N-1)/2}^{(N-1)/2} e^{-j2\pi \frac{mS\sqrt{\epsilon_r}}{\lambda_0} \sin(\theta)} = \frac{\sin(N\pi S\sqrt{\epsilon_r} \sin(\theta) / \lambda_0)}{\sin(\pi S\sqrt{\epsilon_r} \sin(\theta) / \lambda_0)}$$

where  $\epsilon_r$  the relative permittivity of the surrounding medium and  $\lambda_0$  is the free space wavelength.

The key features of the design are the slot length  $L$ , slot width  $W$ , and the slot separation  $S$ . Due to the relatively thick substrate with no coupling lenses, the parameter to optimize not to excite grating lobes within the frequency band of interest, is the slot separation distance  $S$ , which must follow:

$$S \leq \frac{\lambda_{0,\min}}{\sqrt{\epsilon_r}} \left(1 - \frac{1}{N}\right)$$

where  $\lambda_{0,\min}$  is minimum wavelength of operation. With an operating bandwidth of 150-180 GHz (i.e.  $\lambda_{0,\min}=1.7\text{mm}$ ), the spacing must satisfy  $S \leq 460\text{ }\mu\text{m}$ .

Another key design parameter is the length of the slots. Since the design is constrained by the slot separation distance  $S$ , the length of the slots that can used is also constrained. Ideally, for broadband performance, the slot antennas are used at their second resonance where the real part of the slot impedance is relatively constant and its value can be optimized between 20-60  $\Omega$ , when fed at the center of the slot. However, for the slots to operate in the second resonance, the length of the slots needs to be more than  $0.3\lambda_0$ . The grating lobe constraint makes it impossible to operate the slots in their second resonance. Therefore, the slots for the BICEP2 antenna are operational in their first resonance. Unfortunately, the impedance bandwidth of a single slot operating in the first resonance is relatively narrow and the real part of the impedance is very high, in the 100-150  $\Omega$  range, depending on the specific design (caused by a current node at the slot center as shown in Figure 11.42). The impedance can be optimized to somewhat lower-value (50-60  $\Omega$ ) in a “T” slot array configuration. Since the impedance of the detectors used for the BICEP2 instrument is relatively low, in the 20-25  $\Omega$  range, it needs a matching circuit to match the detector impedance with the antenna impedance when the slots are fed at the center. One way to overcome this is to feed the slots off-center. The real part of the impedance of a slot antenna operating at the first resonance decreases as the feed is moved away from the center, towards the edge of the slot. However, that breaks the symmetry of the slot array, leading to cross-polar coupling, and poor cross-polarization performance. The conflicting requirements of low value for the real part of the antenna at first resonance and low cross-polarization performance was addressed by feeding the slots at two points, towards the edge of the slots. This made the antenna a symmetric structure and at the same time providing low value for the real part of the antenna impedance ( $\sim 22\text{ }\Omega$ ), as shown in Figure 11.43c.

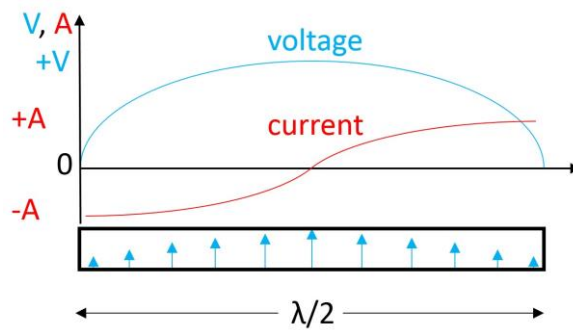


**Figure 11.42.** Current and voltage distribution on a half-wavelength slot. The impedance  $Z = V/I$  is maximum in the center of the slot. The impedance reduces as the feeding point moves away from the center.

Provided that impedances between the microstrip line and slot are well matched, the coupling effectively transmutes the electric fields across the slot into fields. For the microstrip feed lines to match the antenna resistance, the thinnest lines that can be reproducibly fabricated is required (i.e.  $1\mu\text{m}$  as shown in Figure 11.43b). The feed points also have a  $5\text{ }\Omega$  inductive reactance. It is tuned away using series capacitors that shunt current to ground (Figure 11.43c). This inductive reactance is relative stable

across the frequency and that is why a simple capacitor is enough.

The waves from the slots coherently sum in a corporate microstrip feed network. The network first combines incoming signals across rows and then sums the signals from each row in a column tree at the side of the detector. The signals sum in microstrip tee-junctions with proper impedance matching.

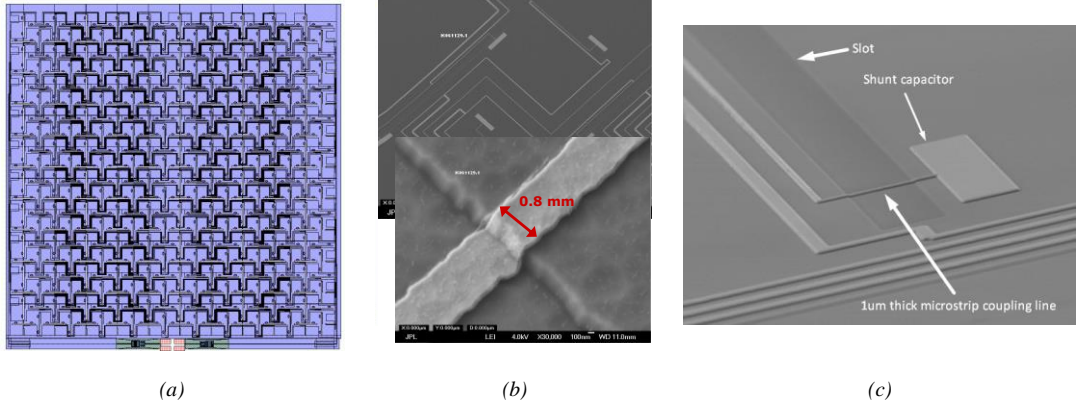


**Figure 11.43.** (a) Layout of BICEP2 slot array. (b) SEM micrograph of the fabricated slot array showing the  $1\mu\text{m}$ -thick microstrip coupling line. (c) SEM micrograph of microstrip crossover and shunt capacitor at a sub-antenna slot.

Each pixel of the phased array consists of  $10 \times 10$  slot arrays for each polarization, 100 horizontal slots and 100 vertical slots, over a  $10\text{mm} \times 10\text{mm}$  area. The slots are excited in-phase with superconducting microstrip transmission lines. There are two transition edge sensor (TES) detectors for each pixel, one for each polarization. The overall slot array is sized to match the  $f/2.2$  camera optics for the BICEP2 instrument.

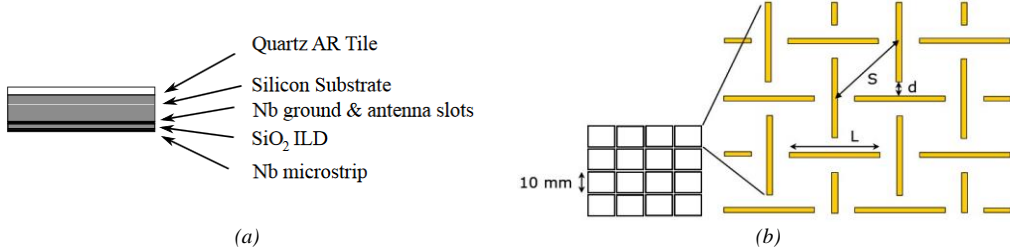


**Figure 11.44.** Schematic diagram of the slot antenna array showing the slots for one pixel. (a) Cross-section of the pixel geometry. (b) Slots position for one pixel. Each pixel is  $10 \text{ mm} \times 10 \text{ mm}$ , and there are  $10 \times 10$  pixels in the focal plane.

For characterization of the dual-polarization slot array, the TES outputs were read out by SQUIDs. To characterize the filter, the TES outputs were read out by SQUIDs. The detector system has an integrated microstrip bandpass filter to define the passband of the instrument. Two separate chips were fabricated and tested, one with the bandpass filter and the other without it. This was done to characterize both the filter and slot antenna designs independently. FTS response of the antenna with integrated bandpass filter and the measured co-polarized beam pattern of the antenna is shown in Figure 11.45.

The slot array is currently integrated into the BICEP2 instrument and is collecting data every day in search of answers about the creation of the Universe, and all these are dictated by the performance of the dual-polarized “T” slot phased array antenna.

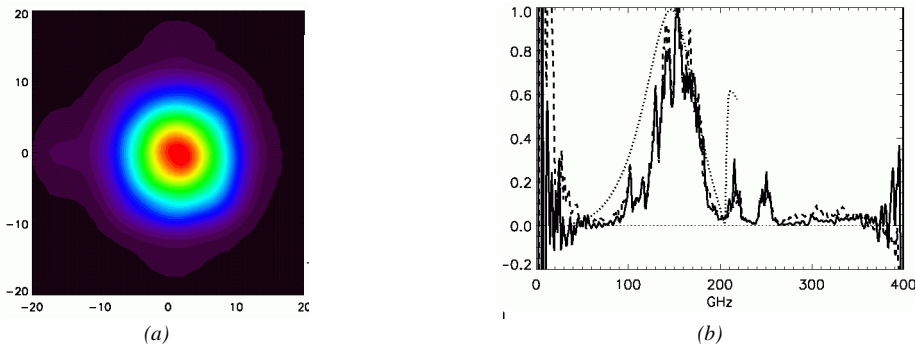


**Figure 11.45.** (a) Measured co-polarized beam pattern. (b) FTS response of the 145GHz slot antenna array.

## 11.7. Conclusion

This chapter discusses the dominant types of antenna used at terahertz frequencies. For waveguide-based systems where polarization content is not a significant concern, diagonal horns are commercially available, simple to integrate into custom designs and have sufficient gaussicity. In planar systems, a substrate integrated lens fed by a double-slot or double-dipole the common choice because of the direct integration, high efficiencies, and relatively simple assembly required.

Because many applications at terahertz are for science instruments, higher performance is often demanded. Spline-profiled and multi-flare angled horns provide excellent performance while still being manufacturable with standard CNC milling processes. Corrugated horns are more challenging to produce, but have been demonstrated up to 340 GHz, with higher frequencies possible. The leaky-wave coupled lens designs demonstrate a step forward in the lens-coupled designs by reducing the aperture size of the lens. This enables batch fabrication of the lenses and higher array densities. Finally, the slot-array described in the final section shows a high-gain, highly polarization sensitive design, enabled by superconducting transmission-lines.

## Acknowledgement

Part of this work was supported by NASA Jet Propulsion Laboratory (JPL), CA. and "National Aeronautics and Space Administration" (NASA). Part of this work was also supported by a Marie Curie International Outgoing Fellowship within the 7<sup>th</sup> European Community Framework Programme.

## References

- [1] A. Love, *Electromagnetic horn antennas*, IEEE Press, 1976.
- [2] P. Clarricoats and A. Olver, *Corrugated Horns for Microwave Antennas*. P. Peregrinus, 1984.
- [3] A. D. Olver, P. J. Clarricoats, A. A. Kishk, and L. Shafai, *Microwave Horns and Feeds*. Institution of Engineering and Technology, 1994.
- [4] T. S. Bird and C. Granet, “Profiled horns and feeds” in L. Shafai et al., “Handbook of Reflector Antennas and Feed Systems: Volume 2 - Feed Systems,” Artech House, 2013.
- [5] P. F. Goldsmith, “Quasioptical systems: Gaussian beam, quasioptical propagation, and applications,” *New York: IEEE Press/Chapman & Hall*, Jan. 1998.
- [6] A. W. Love, “The diagonal horn antenna,” *Microwave J.*, vol. V, pp. 117–122, Mar. 1962.
- [7] J. F. Johansson and N. D. Whyborn, “The diagonal horn as a sub-millimeter wave antenna,” *IEEE Trans. Microw. Theory Tech.*, vol. 40, no. 5, pp. 795–800, May 1992.
- [8] T. Reck, C. Jung-Kubiak, J. Siles, C. Lee, R. Lin, G. Chattopadhyay, I. Mehdi, and K. Cooper, “A silicon micromachined eight-pixel transceiver array for submillimeter-wave radar,” *IEEE Trans. THz Sci. Technol.*, vol. 5, no. 2, pp. 197–206, March 2015.
- [9] P. D. Potter, “A new horn antenna with suppressed sidelobes and equal beamwidths,” *NASA Technical Documents*, Technical report No. 32-354, Feb. 25, 1963.
- [10] P. Kittara, A. Jiralucksanawong, G. Yassin, S. Wangsuya, and J. Leech, “The design of potter horns for THz applications using a genetic algorithm,” *Int. J. Infrared Milli. Waves*, vol. 28, no. 12, pp. 1103–1114, Dec. 2007.
- [11] H. M. Pickett, J. C. Hardy, and J. Farhoodmand, “Characterization of a dual-Mode horn for submillimeter wavelengths,” *IEEE Transactions on Microwave Theory and Techniques*, vol. 32, no. 8, pp. 936–937, Aug 1984.
- [12] J. F. Johansson, “A Gauss-Laguerre Analysis of the Dual-Mode (‘Potter’) Horn,” in *4th Int. Symp. Space Terahertz Technol.*, Apr. 1993, p. 134.
- [13] B. M. Thomas, “Design of corrugated conical horns,” *IEEE Trans. Antenna Propag.*, vol. 26, no. 2, pp. 367–372, 1978.
- [14] C. Granet and G. L. James, “Design of corrugated horns: a primer,” *IEEE Antennas and Propag. Mag.*, vol. 47, no. 2, pp. 76–84, Apr. 2005.
- [15] G. L. James, “Analysis and design of TE<sub>11</sub>-to-HE<sub>11</sub> corrugated cylindrical waveguide mode converters,” *IEEE Trans. Microw. Theory Tech.*, vol. 29, no. 10, pp. 1059–1066, Oct. 1981.
- [16] G. James, “Design of wide-band compact corrugated horns,” *IEEE Trans. Antennas Propag.*, vol. 32, no. 10, pp. 1134–1138, Oct. 1984.
- [17] G. L. James and B. M. Thomas, “TE<sub>11</sub> to HE<sub>11</sub> cylindrical waveguide mode converters using ring-loaded slots,” *IEEE Trans. Microw. Theory Tech.*, vol. 30, no. 3, pp. 278–285, Mar. 1982.
- [18] X. Zhang, “Design of conical corrugated feed horns for wide-band high-frequency applications,” *IEEE Trans. Microw. Theory Tech.*, vol. 41, no. 8, pp. 1263–1274, Aug. 1993.
- [19] A. D. Olver and J. Xiang, “Design of profiled corrugated horns,” *IEEE Trans. Antennas Propag.*, vol. 36, no. 7, pp. 936–940, July 1988.
- [20] R. Gonzalo, J. Teniente, and C. del Rio, “Improved radiation pattern performance of Gaussian profiled horn antennas,” *IEEE Trans. Antennas Propag.*, vol. 50, no. 11, pp. 1505–1513, Nov. 2002.
- [21] G. Gentili, R. Nesti, G. Pelosi, and V. Natale, “Compact dual-profile corrugated circular waveguide horn,” *Electron. Lett.*, vol. 36, no. 6, pp. 486–487, Mar. 2000.
- [22] B. Maffei, et al., “Planck pre-launch status: Hfi beam expectations from the optical optimisation of the focal plane,” *A & A*, vol. 520, p. A12, 2010.

- [23] J. E. McKay, D. A. Robertson, P. A. S. Cruickshank, R. I. Hunter, D. R. Bolton, R. J. Wylde, and G. M. Smith, "Compact wideband corrugated feedhorns with ultra-low sidelobes for very high performance antennas and quasi-optical systems," *IEEE Trans. Antennas Propag.*, vol. 61, no. 4, pp. 1714–1721, Apr. 2013.
- [24] R. W. Haas, D. Brest, H. Mueggenburg, L. Lang, and D. Heimlich, "Fabrication and performance of MMW and SMMW platelet horn arrays," *Int. J. Infrared and Milli. Waves*, vol. 14, no. 11, pp. 2289–2294, 1993.
- [25] M. Kangas, K. Copsey, and P. Lubin, "A modular 100-GHz high-gain scalar corrugated nonbonded platelet antenna," *IEEE Antennas Wireless Propag. Lett.*, vol. 4, pp. 89–92, 2005.
- [26] M. M. Kangas, M. Ansmann, B. Horgan, N. Lemaster, R. Leonardi, A. Levy, P. Lubin, J. Marvil, P. McCreary, and T. Villela, "A 31 pixel flared 100-GHz high-gain scalar corrugated nonbonded platelet antenna array," *IEEE Antennas Wireless Propag. Lett.*, vol. 4, pp. 245–248, 2005.
- [27] L. Lucci, R. Nesti, G. Pelosi, and S. Selleri, "A stackable constant-width corrugated horn design for high-performance and low-cost feed arrays at millimeter wavelengths," *IEEE Antennas Wireless Propag. Lett.*, vol. 11, pp. 1162–1165, 2012.
- [28] J. W. Britton, J. P. Nibarger, K. W. Yoon, J. A. Beall, D. Becker, H.-M. Cho, G. C. Hilton, J. Hubmayr, M. D. Niemack, and K. D. Irwin, "Corrugated silicon platelet feed horn array for CMB polarimetry at 150 GHz," *Proc. SPIE*, vol. 7741, 2010, pp. 77 410T–77 410T–11.
- [29] J. P. Nibarger, J. A. Beall, D. Becker, J. Britton, H.-M. Cho, A. Fox, G. C. Hilton, J. Hubmayr, D. Li, J. McMahon, M. D. Niemack, K. D. Irwin, J. Van Lanen, and K.W. Yoon, "An 84 pixel all-silicon corrugated feedhorn for CMB measurements," *J. Low Temp. Phys.*, vol. 167, no. 3, pp. 522–527, 2012.
- [30] C. Lee, G. Chattopadhyay, E. Decrossas, A. Peralta, I. Mehdi, C. A. Leal-Sevillano, M. A. Pino, and N. Llombart, "Terahertz antenna arrays with silicon micromachined-based microlens antenna and corrugated horns," *Int. Workshop Antenna Technol. (iWAT)*, Mar. 2015, pp. 70–73.
- [31] T. Reck, C. Jung-Kubiak, J. Gill, and G. Chattopadhyay, "Measurement of silicon micromachined waveguide components at 500–750 GHz," *IEEE Trans. THz Sci. Technol.*, vol. 4, no. 1, pp. 33–38, Jan. 2014.
- [32] J. Leech, Boon Kok Tan; G. Yassin, P. Kittara, and S. Wangsuya, "Experimental Investigation of a Low-Cost, High Performance Focal-Plane Horn Array," *IEEE Trans. Terahertz Science Techn.*, vol. 2, no. 1, pp.61–70, Jan. 2012.
- [33] N. Chahat, T. Reck, C. Jung-Kubiak, T. Nguyen, R. Sauleau, and G. Chattopadhyay, "1.9 THz multi-flare angle horn optimization for space instruments," *IEEE Trans. Terahertz Science Technology*, vol. 5, no. 6, pp. 914–921, Nov. 2015.
- [34] N. Chahat, R. E. Hodges, J. Sauder, M. Thomson, E. Peral and Y. Rahmat-Samii, "CubeSat Deployable Ka-band mesh reflector antenna development for Earth science missions," in *IEEE Trans. Antennas Propag.*, vol. 64, no. 6, pp. 2083–2093, June 2016.
- [35] C. Granet, G. L. James, R. Bolton, and G. Moorey, "A smooth-walled spline-profile horn as an alternative to the corrugated horn for wide band millimeter-wave applications," *IEEE Trans. Antennas Propag.*, vol. 52, no. 3, pp. 848–854, Mar. 2004.
- [36] C. Granet, G. L. James, R. Bolton, and G. Moorey, "A smooth-walled spline-profile horn as an alternative to the corrugated horn for wide band millimeter-wave applications," *IEEE Trans. Antennas Propag.*, vol. 52, no. 3, pp. 848–854, Mar. 2004.
- [37] CST Microwave Studio, <https://www.cst.com>.
- [38] A. Rolland, M. Ettorre, M. Drissi, L Le Coq, and R. Sauleau, "Optimization of reduced-size smooth-walled conical horns using BoR-FDTD and genetic algorithm," *IEEE Trans. Antennas and Propag.*, vol. 58, no. 9, pp. 3094–3100, Sept. 2010.
- [39] T. G. Jurgens, J. G. Blaschak, and G. W. Saewert, "Bodies of revolution," in Computational Electrodynamics: The Finite-Difference Time-Domain Method, A. Taflove and S. C. Hagness, Eds.,

3rd ed. Boston, MA: Artech House, 2005, ch. 12, pp. 517–552.

- [40] M. Celuch and W. K. Gwarek, “Industrial design of axisymmetrical devices using a customized solver from RF to optical frequency bands,” *IEEE Microw. Mag.*, vol. 9, no. , pp. 150–159, Dec. 2008.
- [41] G. Godi, R. Sauleau, L. Le Coq, and D. Thouroude, “Design and optimization of three-dimensional integrated lens antennas with genetic algorithm,” *IEEE Trans. Antennas Propag.*, vol. 55, no. 3, pp. 770–775, Mar. 2007.
- [42] G. M. Rebeiz, D. P. Kasilingam, Y. Guo, P. A. Stimson and D. B. Rutledge, “Monolithic millimeter-wave two-dimensional horn imaging arrays,” in *IEEE Trans. Antennas Propag.*, vol. 38, no. 9, pp. 1473–1482, Sep. 1990.
- [43] G. M. Rebeiz, “Millimeter-wave and terahertz integrated circuit antennas,” in *Proc. IEEE*, vol. 80, no. 11, pp. 1748–1770, Nov. 1992.
- [44] D. F. Filipovic, S. S. Gearhart and G. M. Rebeiz, “Double-slot antennas on extended hemispherical and elliptical silicon dielectric lenses,” in *IEEE Trans. Microw. Theory Tech.*, vol. 41, no. 10, pp. 1738–1749, Oct. 1993.
- [45] T. H. Buttgenbach, “An improved solution for integrated array optics in quasi-optical mm and submm receivers: the hybrid antenna,” in *IEEE Trans. Microw. Theory Tech.*, vol. 41, no. 10, pp. 1750–1760, Oct. 1993.
- [46] R. Compton, R. McPhedran, Z. Popovic, G. Rebeiz, P. Tong and D. Rutledge, “Bow-tie antennas on a dielectric half-space: Theory and experiment,” *IEEE Trans. Antennas Propag.*, vol. 35, no. 6, pp. 622–631, Jun. 1987.
- [47] R. DuHamel and D. Isbell, “Broadband logarithmically periodic antenna structures,” *1958 IRE Int. Convention Record*, New York, NY, USA, 1957, pp. 119–128.
- [48] J. Dyson, “The equiangular spiral antenna,” *IRE Trans. Antennas and Propag.*, vol. 7, no. 2, pp. 181–187, Apr. 1959.
- [49] T. H. Buttgenbach, R. E. Miller, M. J. Wengler, D. M. Watson and T. G. Phillips, “A broad-band low-noise SIS receiver for submillimeter astronomy,” in *IEEE Trans. Microw. Theory Tech.*, vol. 36, no. 12, pp. 1720–1726, Dec. 1988.
- [50] D. F. Filipovic, G. P. Gauthier, S. Raman and G. M. Rebeiz, “Off-axis properties of silicon and quartz dielectric lens antennas,” *IEEE Trans. Antennas Propag.*, vol. 45, no. 5, pp. 760–766, May 1997.
- [51] G. Rebeiz, W. Regehr, D. Rutledge, R. Savage and N. Luhmann, “Submillimeter-wave antennas on thin membranes,” *Antennas and Propagation Society International Symposium*, 1987, 1987, pp. 1194–1197.
- [52] D. Rutledge and M. Muha, “Imaging antenna arrays,” in *IEEE Trans. Antennas Propag.*, vol. 30, no. 4, pp. 535–540, Jul. 1982.
- [53] N. Llombart and A. Neto, “THz Time-Domain Sensing: The Antenna Dispersion Problem and a Possible Solution,” *IEEE Trans. THz Sci. Technol.*, vol. 2, no. 4, pp. 416–423, Jul. 2012.
- [54] A. Neto, N. Llombart, J. J. A. Baselmans, A. Baryshev and S. J. C. Yates, “Demonstration of The Leaky Lens Antenna at Submillimeter Wavelengths,” *IEEE Trans. THz Sci. Technol.*, vol. 4, no. 1, pp. 26–32, Jan. 2014.
- [55] N. Llombart, G. Chattopadhyay, A. Skalare and I. Mehdi, “Novel Terahertz Antenna Based on a Silicon Lens Fed by a Leaky Wave Enhanced Waveguide,” *IEEE Trans. Antennas Propag.*, vol. 59, no. 6, pp. 2160–2168, Jun. 2011.
- [56] N. Llombart *et al.*, “Silicon Micromachined Lens Antenna for THz Integrated Heterodyne Arrays,” *IEEE Trans. THz Sci. Technol.*, vol. 3, no. 5, pp. 515–523, Sep. 2013.
- [57] M. Alonso-DelPino *et al.*, “Design Guidelines for a Terahertz Silicon Micro-Lens Antenna,” *IEEE Antennas and Wireless Propag. Lett.*, vol. 12, no. , pp. 84–87, 2013.

- [58] D. R. Jackson and A. A. Oliner, "A leaky-wave analysis of the high-gain printed antenna configuration," in *IEEE Trans. Antennas Propag.*, vol. 36, no. 7, pp. 905-910, Jul. 1988.
- [59] A. Neto, "UWB, Non Dispersive Radiation From the Planarly Fed Leaky Lens Antenna— Part 1: Theory and Design," *IEEE Trans. Antennas Propag.*, vol. 58, no. 7, pp. 2238-2247, Jul. 2010.
- [60] N. Llombart, A. Neto, G. Gerini, M. Bonnedal and P. De Maagt, "Impact of Mutual Coupling in Leaky Wave Enhanced Imaging Arrays," in *IEEE Trans. Antennas Propag.*, vol. 56, no. 4, pp. 1201-1206, Apr. 2008
- [61] Meide Qiu, G. V. Eleftheriades and M. Hickey, "A reduced surface-wave twin arc-slot antenna element on electrically thick substrates," *Proc. IEEE AP-S Soc. Int. Symp.*, Boston, MA, USA, 2001, pp. 268-271, vol.3.
- [62] C. Lee, G. Chattopadhyay, K. Cooper and I. Mehdi, "Curvature control of silicon microlens for THz dielectric antenna," *37th Int Conf. Infrared Milli. THz Waves (IRMMW-THz)*, Wollongong, NSW, 2012, pp. 1-2.
- [63] C. Lee, G. Chattopadhyay, M. Alonso-delPino and N. Llombart, "6.4 mm Diameter silicon micromachined lens for THz dielectric antenna," *39th Int. Conf. Infrared Milli. THz waves (IRMMW-THz)*, Tucson, AZ, 2014, pp. 1-1.
- [64] B. Fong, J. Colburn, J. Ottusch, J. Visher, and D. Sievenpiper, "Scalar and tensor holographic artificial impedance surfaces," *IEEE Trans. Antennas Propag.*, vol. 58, no. 10, pp. 3212–3221, Oct. 2010.
- [65] G. Minatti, M. Faenzi, E. Martini, F. Caminita, P. De Vita, D. González-Ovejero, M. Sabbadini, and S. Maci, "Modulated metasurface antennas for space: Synthesis, analysis and realizations," *IEEE Trans. Antennas Propag.*, vol. 63, no. 4, pp. 1288–1300, Apr. 2015.
- [66] D. Sievenpiper, J. Colburn, B. Fong, J. Ottusch, and J. Visher, "Holographic artificial impedance surfaces for conformal antennas," *Proc. IEEE AP-S Soc. Int. Symp.*, vol. 1B, 2005, pp. 256–259 vol. 1B.
- [67] A. Oliner and A. Hessel, "Guided waves on sinusoidally-modulated reactance surfaces," *IRE Trans. Antennas Propag.*, vol. 7, no. 5, pp. 201–208, Dec. 1959.
- [68] G. Chattopadhyay, "Technology, capabilities, and performance of low power terahertz sources," *IEEE Trans. THz Sci. Technol.*, vol. 1, no. 1, pp. 33–53, Sep. 2011.
- [69] M. Esquius-Morote, J. Gomez-Diaz, and J. Perruisseau-Carrier, "Sinusoidally modulated graphene leaky-wave antenna for electronic beamscanning at thz," *IEEE Trans. THz Sci. Technol.*, vol. 4, no. 1, pp. 116–122, Jan. 2014.
- [70] C. Jung, B. Thomas, C. Lee, A. Peralta, J. Gill, K. Cooper, G. Chattopadhyay, E. Schlecht, R. Lin, and I. Mehdi, "Compact submillimeter-wave receivers made with semiconductor nanofabrication technologies," *Proc. IEEE Int. Microw. Symp. (IMS)*, Jun. 2011, pp. 1–4.
- [71] D. González-Ovejero, T. J. Reck, C. D. Jung-Kubiak, M. Alonso-DelPino, and G. Chattopadhyay, "Silicon micromachined modulated metasurface antennas in the terahertz range," in *Proc. 10th Eur. Conf. Antennas Propag.*, 2016, pp. 1–4.
- [72] D. González-Ovejero, T. J. Reck, C. D. Jung-Kubiak, M. Alonso-DelPino, and G. Chattopadhyay, "A class of silicon micromachined metasurface for the design of high-gain terahertz antennas," in *Proc. IEEE AP-S Soc. Int. Symp.*, 2016, pp. 1–4.
- [73] R. King, D. V. Thiel, and K. Park, "The synthesis of surface reactance using an artificial dielectric," *IEEE Trans. Antennas Propag.*, vol. 31, no. 3, pp. 471–476, May 1983.
- [74] H. Bilow, "Guided waves on a planar tensor impedance surface," *IEEE Trans. Antennas Propag.*, vol. 51, no. 10, pp. 2788–2792, Oct. 2003.
- [75] D. González-Ovejero and S. Maci, "Gaussian ring basis functions for the analysis of modulated metasurface antennas," *IEEE Trans. Antennas Propag.*, vol. 63, no. 9, pp. 3982–3993, Sep. 2015.
- [76] ANSYS Inc., "HFSS, Version 15," Pittsburgh, PA, 2015.

- [77] A. Tang et al., “A CMOS D-Band Transmitter with IF Envelope Feed-Forward Pre-Distortion and Injection Locked Frequency Tripling Synthesizer,” *IEEE Trans. Microwave Theory Tech.*, vol. 60, no. 12, Dec 2012, pp. 4129–37.
- [78] A. Tang et al., “A Low Overhead Self-Healing Embedded System for Ensuring High Performance Yield and Long-Term Sustainability of a 60GHz 4Gb/s Radio-on-a-Chip” *IEEE Int'l. Solid-State Circuits Conf. Digest of Tech. Papers*, Feb 2012, pp. 316–18.
- [79] N. Chahat, A. Tang, C. Lee, R. Sauleau, and G. Chattopadhyay, “Efficient CMOS systems with beam-lead interconnects for space instruments,” *IEEE Trans. Terahertz Science Technology*, vol. 5, no. 4, pp. 637-644, July 2015.
- [80] A. Tang, N. Chahat, et al., “A 65nm CMOS 140 GHz 27.3 dBm EIRP transmit array with membrane antenna for highly scalable multi-chip phase arrays,” *Proc. IEEE Int. Microw. Sym. (IMS)*, Tampa, FL, 2014.
- [81] A. Tang and N. Chahat, “CMOS mm-wave transceiver techniques beyond 50 GHz,” *Proc. IEEE Global Conf. Signal Inf. Process. (GlobalSIP)*, Austin, TX, 2013, pp. 715-718.
- [82] A. Tang et al., “CMOS (Sub)-mm-Wave System-on-Chip for exploration of deep space and outer planetary systems,” *Proc. IEEE Custom Integrated Circuits Conf.*, San Jose, CA, 2014.
- [83] A. Tang et al., “A 95 GHz centimeter scale precision confined pathway system-on-chip navigation processor for autonomous vehicles in 65nm CMOS,” *Proc. IEEE Int. Microw. Sym. (IMS)*, Phoenix, AZ, 2015, pp. 1-3.
- [84] R. R. Cladwell and M Kamionkowski, “Echoes from the Big Bang,” *Scientific American*, pp. 38-43, January 2001.